Filament formation drives catalysis by glutaminase enzymes important in cancer progression

Shi Feng[1], Cody Aplin[1], Thuy-Tien T. Nguyen[1], Shawn K. Milano[1], and Richard A. Cerione[1,2*]

[1]Department of Chemistry and Chemical Biology, Cornell University, Ithaca, New York, 14853

[2]Department of Molecular Medicine, Cornell University, Ithaca, New York, 14853

*Corresponding author: rac1@cornell.edu

The glutaminase enzymes GAC and GLS2 catalyze the hydrolysis of glutamine to glutamate, satisfying the 'glutamine addiction' of cancer cells. They are the targets of anti-cancer drugs; however, their mechanisms of activation and catalytic activity have been unclear. Here we demonstrate that the ability of GAC and GLS2 to form filaments is directly coupled to their catalytic activity and present their cryo-EM structures which provide an unprecedented view of the conformational states essential for catalysis. Filament formation guides an 'activation loop' to assume a specific conformation that works together with a 'lid' to close over the active site and position glutamine for nucleophilic attack by an essential serine. Our findings highlight how ankyrin repeats on GLS2 regulate enzymatic activity, while allosteric activators stabilize, and clinically relevant inhibitors block, filament formation that enables glutaminases to catalyze glutaminolysis and support cancer progression.

Metabolic reprogramming is well-established as a hallmark of cancer progression[1-3]. A shift in the metabolic requirements of cancer cells compared to normal cells, known as the Warburg effect[4-6], results in their dependence on glutamine as an energy source in addition to glucose.

Glutamine catabolism, which starts with the hydrolysis of glutamine to glutamate catalyzed by the glutaminase family of enzymes, becomes highly upregulated in cancer cells to compensate for the uncoupling of the glycolytic pathway from the TCA cycle due to the Warburg effect, thus providing the biosynthetic precursors necessary for their enhanced proliferation and survival[7-10]. Given the resulting glutamine addiction of cancer cells, the development of allosteric small molecule inhibitors that target glutaminase activity is being examined as a potential therapeutic strategy to block tumor progression in various malignancies including aggressive breast, lung, and pancreatic cancers, as well as for their effectiveness when combined with other anti-cancer drugs[11-16]. The glutaminases are encoded by two independent genes, *gls* and *gls2*. *Gls* encodes kidney-type glutaminase (KGA) and its C-terminal truncated splice variant glutaminase C (GAC) which is highly expressed in many cancers. *Gls*2 encodes only one active isozyme, liver-type glutaminase (LGA; from hereon designated as GLS2). While GLS2 has been suggested to serve as a tumor suppressor by directly binding the Rac GTPase and promoting ferroptosis in hepatocellular carcinoma[17,18], it has also been shown to be necessary for cancer progression as we and others have found that it is essential for the growth and survival of luminal subtype receptor-positive breast cancer cells[9,19]. Moreover, GLS2 is highly expressed in ovarian, lung and colorectal cancers and has been suggested to compensate for GAC downregulation or inhibition[10,20].

All glutaminase enzymes share a catalytic domain containing identical active site residues and a conserved mechanism for hydrolyzing glutamine to glutamate[21-23]. The catalytic efficiency of the glutaminase enzymes is markedly increased in the presence of inorganic phosphate *in vitro*[24,25], although the concentration of this allosteric activator required to promote their enzymatic activity may not be attainable in many physiological contexts suggesting that other anionic activators likely exist. Understanding more about the catalytic mechanism used by these enzymes and the structural

47 changes that they need to undergo to become activated will be important for further developing
48 drug candidates that effectively block their enzymatic activity. Potent inhibitors targeting GAC are
49 available, the most effective being the BPTES/CB-839 group of compounds with CB-839 and
50 others such as UPGL004 having nanomolar binding affinity[26,27]. However, the development of
51 specific and potent allosteric inhibitors of GLS2 has not been as successful, as currently the best
52 examples are the 968-class of molecules[9,15] which have binding affinities for the enzyme only in
53 the micromolar range.

54 It has been known for some time that a number of metabolic enzymes assemble into filament-
55 like structures which may play a key regulatory role in their catalytic activity, but in the majority
56 of cases, the importance of these higher order structures for enzyme regulation and function has
57 not been definitively established[28]. Recently it has been shown that GAC can assemble into long
58 filaments in cells to facilitate efficient glutamine consumption[29]. While the formation of these
59 oligomeric supramolecular assemblies has been suggested to be associated with the *in vitro*
60 activation of GAC by inorganic phosphate[30,31], an essential question concerns if the assembly of
61 such higher-order oligomers is in fact directly coupled to catalytic activity. Moreover, it has yet
62 to be established whether filament formation is a common mechanism for all glutaminase
63 isozymes. This is an especially important question for GLS2 given that it might be differentially
64 regulated due to the presence of ankyrin repeats, which are absent on the C-terminal truncated
65 splice variant GAC[32,33], and because it can sometimes exert the opposite functional effects from
66 GAC on cancer progression.

67 In this study, we show that GAC as well as GLS2 undergoes filament formation in the presence
68 of the substrate glutamine and the activator inorganic phosphate, with the assembly of these higher-
69 order oligomers being directly coupled to glutamine hydrolysis and product (glutamate) release.

70 We further present the high-resolution structures for a GAC filament bound to its anionic activator
71 inorganic phosphate (Pi), and for a constitutively active GLS2 filament, determined by cryo-
72 electron microscopy (cryo-EM). These novel filamentous structures now provide us with several
73 important new insights into how key regions of the glutaminases and their essential residues are
74 positioned to achieve maximal catalytic activity, as well as shed light on how anionic activators,
75 allosteric inhibitors, and ankyrin repeats can impart their regulatory effects on enzymes that play
76 critical roles in cancer progression.
77
78 **RESULTS**
79
80 **General structural features of the glutaminase enzymes**
81 Several high-resolution X-ray structures for KGA and GAC have been reported; however,
82 thus far, there has not been a structural determination for the full-length apo-GLS2 protein.
83 Therefore, we obtained a cryo-EM structure for wildtype, full-length GLS2. Figs. 1a and 1b show
84 the 3.1 Å structure of the human apo-GLS2 tetramer and the relative positions of the key regions
85 for catalytic activity (i.e., the 'activation loop', the catalytic site, and the 'lid loop' that opens and
86 closes over the catalytic domain)[23]. Fig. 1a also highlights the three major domains of a monomeric
87 unit of GLS2, namely, the N-terminal region, C-terminal ankyrin repeats, and the highly conserved
88 catalytic site. The overall structure of the apo-GLS2 tetramer strongly resembles those of the apo-
89 forms of GAC and KGA solved by X-ray crystallography (Fig. 1a)[24,33], and the active sites within
90 each GLS2 subunit show the same general features as a previously reported crystal structure of the
91 enzyme's limit catalytic domain as well as those of GAC[22] (Fig. 1c). The fact that these structural
92 features are highly conserved among the glutaminase enzymes indicate that they share a common

93 catalytic mechanism. We analyzed several key structural elements in the catalytic domain of GLS2
94 that have been suggested to exert an allosteric regulation of glutaminase activity. The stretch of
95 residues Gly248-Glu258, which has been shown to play an essential role in catalysis and thus
96 referred to as the 'activation loop'[23,34], is disordered and flexible in the GLS2 structure (Fig. 1b).
97 In GAC, this loop contains the binding site for the BPTES class of allosteric inhibitors which
98 includes CB-839, a drug candidate that has been in clinical trials[26]. The loop forms a stable,
99 inactive conformation when bound to BPTES and to its more potent analogs, CB-839 (not shown)
100 and UPGL0004[35,36] (Extended Data Fig. 1). However, the activation loop of GLS2 differs from
101 KGA and GAC by two residues, rendering GLS2 insensitive to these inhibitors[24]. In addition,
102 residues Tyr182-Lys188 in GLS2, which correspond to a loop in KGA and GAC forming a 'lid'
103 that needs to close over bound substrates for catalysis to occur, are also flexible like the activation
104 loops in the GLS2 structure. This is in contrast to the previously reported crystal structure of the
105 GLS2 limit catalytic domain, which showed the lid region adopting an "open" conformation[22].
106

107 **Glutaminase filament formation is directly coupled to catalytic activity**

108 The glutaminase enzymes have been shown to undergo dimer-to-tetramer transitions upon
109 binding activators such as inorganic phosphate (Pi)[25,37], as a necessary step for enzymatic activity.
110 However, high-resolution X-ray crystal structures of the tetrameric forms of glutaminase enzymes
111 have failed to shed light on the critical changes in their catalytic sites that promote the hydrolysis
112 of glutamine to glutamate. In fact, the positions of the catalytic residues in the structures obtained
113 for glutaminase dimers and tetramers are virtually identical[25,38]. Therefore, these findings further
114 raised the possibility that GAC needs to form a higher-order oligomeric state in cells, resulting in
115 a filament-like structure, in order for catalysis to occur[29,31,39]. Given the structural similarities

116 between GAC and GLS2, it might be expected that GLS2 would undergo a similar structural
117 transition, although GLS2 can in some cancers exhibit the opposite effects from GAC by acting as
118 a tumor suppressor rather than a promoter raising the possibility that it might exhibit distinct
119 structural features. Thus, we set out to see if a filament-like structure is indeed formed by GLS2
120 as well as GAC and whether its formation is coupled to catalysis.

121 Using negative stain electron microscopy (EM), we visualized the structural changes that
122 recombinant wild-type human GAC and GLS2 undergo upon the addition of the substrate
123 glutamine and the anionic activator Pi under catalytic conditions (Figs. 2a and 2b). GAC
124 immediately formed filaments with the addition of the substrate and activator, similar in
125 appearance to those described in a previous report[31], and the same was true for GLS2, thus
126 indicating that filament formation is common to all glutaminase enzymes. However, once the
127 substrate glutamine was fully converted to product (glutamate), the filaments disassembled into
128 tetramers as shown for GLS2 in Fig. 2c, supporting the idea that filament formation is coupled to
129 catalytic turnover.

130 To further establish a direct connection between filament formation and enzyme catalysis, we
131 took advantage of right-angle light scattering (RALS) to monitor the assembly of these higher
132 order oligomers in real time. Fig. 2d shows an example for GLS2. Upon adding Pi and glutamine
133 to the enzyme, there was an immediate, marked increase in light scattering. The increase in RALS
134 peaked within minutes and was followed by a rapid decline, with the decrease in the peak matching
135 the time scale for the dissociation of GLS2 filaments as visualized by negative stain EM. The
136 maximal increase in RALS required both the substrate glutamine and the anionic activator Pi and
137 was not detected in the absence of substrate (Extended Data Fig. 2a), demonstrating that the
138 changes in RALS accurately reflect the association and dissociation of filaments. Subsequent

139 additions of glutamine to the enzyme re-established filament formation, with substrate
140 consumption again resulting in filament disassembly (Fig. 2d). The addition of the product,
141 glutamate, was unable to trigger filament formation. Taken together, these results further indicate
142 that filament assembly-disassembly is directly coupled to substrate binding and catalytic turnover.
143 Mutations that result in the constitutive activation of the glutaminase enzymes were then
144 examined by negative stain EM and RALS for their effects on filament formation. Changing a key
145 lysine residue (i.e., Lys320 in GAC and Lys253 in GLS2) to alanine within the activation loop
146 gives rise to constitutively active enzymes, with their activity matching that of the wild-type
147 enzyme measured in the presence of the anionic activator Pi[38]. The RALS profile and negative
148 stain images showed that glutamine addition alone was sufficient to drive constitutively active
149 forms of human GAC (K320A) and GLS2 (K253A) to form filaments, as the activation loop
150 substitution effectively substitutes for the requirement of an anionic activator (Extended Data Figs.
151 2b-d). Again, the product glutamate was unable to drive filament assembly, nor did the presence
152 of high concentrations of glutamate prior to glutamine addition have any effect on the ability of
153 substrate to induce filament formation (Extended Data Fig. 2d). The lifetime of the higher order
154 oligomeric filaments, as readout by RALS, was a direct function of the substrate (glutamine)
155 concentration, as shown for GLS2 (Extended Data Fig. 2e). Likewise, the length of the filaments
156 that formed were a function of substrate concentration and consisted of as many as 30 tetramers
157 (Extended Data Fig. 2f), most likely because the greater the substrate concentration, the longer the
158 time required for its total consumption and thus the ability to increase the growth of the filaments.
159 This is again consistent with filament assembly-disassembly being directly coupled to enzyme
160 activation and catalytic turnover. We then reasoned that conditions that allow substrate binding
161 and filaments to form, but do not permit product (glutamate) formation, should result in the

162 persistence of these higher order oligomers. Therefore, we tested this prediction by taking
163 advantage of our earlier finding that substituting an essential tyrosine residue within the enzyme
164 active site of GAC does not disrupt substrate (glutamine) binding but prevents its hydrolysis to
165 glutamate[25,34]. As shown in Fig. 2e, the RALS signal for GAC (Y466W) did not diminish over
166 time.
167
168 **Structural determinations of GAC and GLS2 filaments**
169 We determined a 3.3 Å cryo-EM structure of the human GAC (Y466W) mutant which,
170 because it is defective for hydrolyzing glutamine to glutamate, assembled into a stable filament
171 upon binding substrate and the anionic activator phosphate (Pi)[25,34]. Each successive tetramer is
172 rotated ~51 degrees relative to the filament axis with the helical rise of ~68 Å (Figs. 3a, b). We
173 also obtained a 3.3 Å cryo-EM structure of the constitutively active recombinant human GLS2
174 (K253A) mutant that formed a filament immediately after the addition of glutamine alone (and
175 prior to substrate depletion), as this mutant does not require an anionic activator to be catalytically
176 competent (Figs. 3c, d). The tetramers are arranged in a side-by-side architecture and each
177 successive tetramer is rotated ~48 degrees relative to the filament axis, with the helical rise of ~66
178 Å (Fig. 3d). These structures for activated glutaminase enzymes differed from the previously
179 proposed end-to-end double helix model for GAC filament formation[31]. In both the GAC and
180 GLS2 filament structures, each tetramer interacts with its immediate neighbor through an interface
181 of six alpha helices on the lateral side of the catalytic domain near the lid loop that closes over the
182 substrate binding site (Figs. 3e, f). Within this highly conserved interface burying about 710 $Å^2$
183 and 752 $Å^2$ of solvent-accessible area on GAC and GLS2, respectively, Phe355 in GAC (Phe288
184 in GLS2), together with Phe373 (Phe306 in GLS2), Phe378 (Phe311 in GLS2), Asp412 (Asp345

185 in GLS2), and Gln416 (Gln349 in GLS2) from one subunit form an intricate interacting network
186 with Asn375 (Asn308 in GLS2) and Gln379 (Gln312 in GLS2) from the subunit of an adjacent
187 tetramer (Figs. 3g, h).

188 When comparing the filament structures with those for the corresponding tetrameric apo-
189 enzymes described above (Figs. 1, and Extended Data Fig. 1), we found striking differences in the
190 conformation of the activation loops and the lids. The activation loops in both the GAC and GLS2
191 tetramers, either in their apo-, substrate-bound, or product-bound states, are highly flexible and
192 cannot be resolved, except when GAC is bound to the BTPES class of inhibitors (Extended Data
193 Fig. 1). This led us to originally suspect that a flexible rather than stabilized activation loop was
194 essential for the catalytic activity of these enzymes. However, in the substrate- and Pi-bound GAC
195 filament, as well as in the constitutively active substrate-bound GLS2 filament structure, the
196 activation loops are well resolved and adopt a conformation distinct from the inhibitor-induced
197 state in GAC (Figs. 3e, f, and Extended Data Fig. 1).

198 The first significant conformational change involving the activation loops of the GAC and
199 GLS2 filaments, compared to their positions in the apo-enzymes, resulted in a new motif
200 designated here as the 'phenylalanine-tyrosine lock' in GAC and the 'tyrosine lock' in GLS2.
201 These residues lock-in the substrate at the conserved active sites (Figs. 4a, b). In each dimer within
202 a tetrameric unit comprising the filament structures of GAC and GLS2, Glu325 in GAC (Glu258
203 in GLS2) within the activation loop of one monomer subunit forms a new salt bridge with Arg317
204 (Arg250 in GLS2) from the activation loop of the adjacent monomer subunit (Figs. 4c, d). In
205 solving the cryo-EM structure for the GAC(Y466W) filament in the presence of glutamine and Pi,
206 we were able to identify the Pi binding site within the dimer-dimer interface of each tetrameric
207 unit where it interacts with Lys320 and thereby stabilizes the activation loop (Fig. 4c, and Extended

208 Data Fig. 3, left panel). This helps to explain how the binding of Pi to a GAC(F327W) mutant is
209 able to induce an increase in Trp327 fluorescence within the activation loops of the enzyme[40].
210 Conversely, in the absence of Pi and substrate, the activation loops of the enzyme are flexible and
211 therefore are not visualized. Thus, the activation loops of each dimer within the filament fold in a
212 compact manner, thereby bringing Phe318 of GAC (Tyr251 of GLS2) from each loop closer to the
213 active site (Fig. 4c). In the apo-enzyme structures, Arg387 of GAC and Arg320 in GLS2 face
214 toward the active site and prevent glutamine from being 'locked in'. However, in the filament
215 structure of GAC, Pi interacts with Arg387, enabling it to form a salt bridge with Glu397 at the
216 dimer-dimer interface (Figs. 4c, d), which together with the interactions of Pi with Tyr394 and
217 Lys398 (Extended Data Fig. 4a), may be necessary for the glutaminase enzymes to undergo the
218 dimer-to-tetramer transition, a prerequisite for filament formation and catalytic activity.
219 Interestingly, in the filament structure for the constitutively active GLS2 mutant, Arg320 (which
220 corresponds to Arg 387 in GAC) forms the same type of salt bridge in the absence of Pi, as that
221 seen when Pi binds to GAC(Y466W). The formation of these Arg-Glu salt bridges, together with
222 the substitution of a less bulky alanine residue for lysine, allows the movement of the activation
223 loops into a space that otherwise would only occur when Pi binds, and likely explains why the
224 Lys-to-Ala substitutions within the loops yield enzymes that no longer require the binding of an
225 anionic activator.

226 When comparing the filament structures with those of the apo-enzyme, a second significant
227 conformational change involves the lid loops, resulting in the insertion of Tyr249 of GAC (Tyr182
228 of GLS2) into the active site pockets. These two conformational rearrangements involving the
229 activation and lid loops fully close off the active site in each subunit, acting as a 'Phe-Tyr lock' in
230 GAC and a 'Tyr lock' in GLS2, effectively locking the substrate glutamine into an optimal

231 orientation proximal to the residues essential for catalysis (Figs. 4a, b). Moreover, the insertion of
232 the phenyl ring of Phe318 of GAC (Tyr251 in GLS2) brings it within ~5 Å of Lys289 (Lys222 in
233 GLS2), as shown for GAC in the right panel of Extended Data Fig. 3 and GLS2 in Fig. 4e, thereby
234 enabling a cation-π interaction that orients and increases the basicity of a key active site lysine
235 residue. This enables the lysine residue to effectively deprotonate an active site serine (i.e., Ser286
236 in GAC and Ser219 in GLS2), which undergoes a nucleophilic attack and forms a tetrahedral
237 intermediate with glutamine. Hydrolysis can then occur following this initial reaction to form
238 glutamate and ammonia[41].

239 An additional conformational change that occurs specifically in the constitutively active GLS2
240 filament structure, when compared to the tetrameric apo-enzyme, results in a new hydrogen
241 bonding network introduced by the activation loops. Hydrogen bonds that form between Arg250
242 and Asp400 of GLS2 appear to 'stretch' the alpha helix containing Asp400, causing Tyr399 on the
243 N-terminal end of the alpha helix to insert further into the active site where the substrate binds
244 (Fig. 4f). Following the insertion of Tyr399, Glu258 from the adjacent dimer forms a hydrogen
245 bond with Lys440, which displaces the loop containing Lys440, and therefore makes space for the
246 insertion of Tyr399. As a result, Tyr399 is now in close proximity to both Lys222 and the substrate,
247 which is necessary for catalysis. Interestingly, the corresponding tyrosine residue in apo-GAC
248 (Y466W) is already inserted into the active site (Extended Data Fig. 4b), i.e., identical to its
249 position in the GAC and GLS2 filament structures. Because this catalytic residue is properly
250 positioned in the active site even in the apo- or 'resting' state of GAC, it might contribute, together
251 with the absence of ankyrin repeats (see below), to GAC having a significantly higher specific
252 activity compared to GLS2. Collectively, these unprecedented visualizations of the interactions

253 within the active sites of the GAC and GLS2 filaments upon the binding of substrate now provide
254 new insights into the mechanisms by which the glutaminase enzymes catalyze glutaminolysis.
255

256 **A mechanism for glutaminase activation coupled to filament formation**

257 The high-resolution glutaminase filament structures and RALS data presented here show how
258 glutaminase filament formation is coupled to catalysis. In the apo-enzymes, the lid loops do not
259 adopt a fixed conformation and are highly flexible. Such flexibility would likely introduce steric
260 clashes at the tetramer-tetramer interfaces within the filament, thereby preventing filament
261 formation (Fig. 5a, right panel). Upon binding to the enzyme, the substrate forms hydrogen bonds
262 with Glu381 in GAC and Glu314 in GLS2, resulting in the movement of these residues toward the
263 active site (Extended Data Figs. 5a, b, left panels). As shown for GLS2, this enables the alpha helix
264 containing residues Asn308 to Thr317 to move inward, resulting in additional interactions between
265 Thr310 and Gln185, and between Ser313 and Pro184 on the lid loop (Extended Data Fig. 5b, left
266 panel). These two sets of interactions, and those which occur between Tyr249 and Phe318 in GAC,
267 and between Tyr182 and Tyr251 in GLS2, with glutamine stabilize the lid loop in a conformation
268 that together with the activation loop effectively locks-in the substrate. This is necessary for
269 catalysis, as well as exposes the filament interface, therefore allowing additional tetramers to
270 contribute to the growth of the higher-order oligomer (Fig. 5a, left panel). Reciprocally, it is the
271 binding of tetramers to form the enzyme filament that restricts the flexibility of the lids and allows
272 them to adopt a conformation that closes over the substrate binding sites, thus enabling catalysis
273 to occur. Following a catalytic turnover, the product glutamate no longer interacts with the active
274 site tyrosine and glutamic acid residues and thus has a relatively low affinity for the enzyme. Upon
275 its dissociation, the activation loops and the lids becoming highly flexible again to await the next

276 substrate binding event. When all the available substrate is consumed, the lids are not able to be
277 restrained which disrupts the filament interface and gives rise to the dissociation of the filament
278 back to tetramers (Fig. 5a, right panel). The missing density of the lid loop of the terminal tetramer
279 in the cryo-EM map for the constitutively active GLS2 (K253A) filament represents a snapshot of
280 this detachment (Extended Data Fig. 5b, right panel) that occurs following catalytic turnover and
281 product release. However, in the case of the GAC (Y466W) mutant, which binds Pi and substrate
282 but cannot undergo catalysis, the filament persists (Fig. 2e) and now the density of the lid loop
283 within the terminal tetramer of the filament structure remains intact (Extended Data Fig. 5a, right
284 panel).

285 Given that filament formation is directly coupled to glutaminase activation, it might then be
286 expected that small molecule inhibitors that prevent the glutaminases from undergoing the
287 conformational transitions necessary for their activation would negatively impact their ability to
288 assemble into these higher order oligomeric structures. We therefore examined the effects of two
289 allosteric glutaminase inhibitors, UPGL0004 and 968, on filament formation. UPGL004 is a potent
290 member of the BPTES-class of compounds and specifically targets GAC[27,36] by binding to the
291 activation loops (Extended Data Fig. 1) and trapping them in a stable conformational state that
292 prevents their movements into the active sites and from working together with the lid loops to
293 establish the filament interface and lock-in the substrate to undergo catalytic turnover. Thus, we
294 found that while the vehicle control (DMSO) did not interfere with the ability of GAC (Y466W)
295 to form filaments within 30 seconds which persisted through 30 minutes as visualized by negative
296 stain EM (Figs. 5b, c), UPGL004 addition immediately blocked their assembly (Fig. 5d). The
297 BPTES-class of compounds are ineffective against GLS2 because of subtle differences in their
298 activation loops from those of GAC[24]. However, 968 is a small molecule inhibitor that effectively

299 inhibits GLS2 catalytic activity[9]. It appears to bind at the activation loops of GLS2 based on the
300 density we observed for the cryo-EM structure obtained for the 968-GLS2 complex, but without
301 overlapping the binding sites for either the BPTES-class of inhibitors nor Pi (Extended Data Fig.
302 6a), consistent with kinetic analyses from our laboratory[14]. Rather, upon binding to GLS2, 968
303 would block the salt bridge that forms between Arg258 on one activation loop and Glu250 on an
304 adjacent activation loop, thereby preventing the substrate from being locked in at the catalytic site.
305 This could also potentially weaken the interactions between GLS2 dimers to form tetramers, as we
306 have observed by cryo-EM 2D classifications where 968 treatment results in the appearance of
307 some dimeric enzyme particles (Extended Data Fig. 6b). Collectively, these effects would be
308 expected to prevent the formation of filaments that are required for optimal catalysis, which is
309 what we observed by negative stain EM in Figs. 5e and 5f. Likewise, mutation of a key residue
310 within the tetramer-tetramer interface necessary for filament formation (e.g. Asn 308 in GLS2),
311 significantly reduces their size (Fig. 5g) with a corresponding decrease in catalytic activity
312 (Extended Data Fig. 6c). Together, these findings further reinforce the conclusion that the
313 formation of glutaminase filaments is an essential step for enzyme activation and to achieve
314 maximal catalytic turnover.
315

316 **The role of the ankyrin repeat motif in GLS2**

317 The C-terminal region of GLS2 contains an ankyrin repeat motif consisting of three pairs of
318 helical bundles located on the distal ends of the tetramer, which is absent in GAC (Figs. 6a, b).
319 The ankyrin repeats in GLS2 appear to exert a negative regulation of catalytic activity, despite
320 being approximately 70 Å away from the active sites in each subunit. The KGA isoform of GLS
321 also contains ankyrin repeats and has a much lower specific activity than its C-terminal truncated

322 splice variant GAC; moreover, truncated forms of KGA lacking these repeats show increased
323 specific activity[33]. Each GLS2 dimer within a tetrameric unit shares an ankyrin repeat bundle
324 connected to the catalytic domain through a flexible linker. Interestingly, the ankyrin repeats are
325 highly asymmetric. Instead of showing a symmetrical occupancy of the area between the N-
326 terminal motifs of adjacent monomeric units within a tetramer, they show a preferential occupancy
327 on one particular side (Extended Data Fig. 7). As described above, the activation loops within each
328 dimer unit comprising the filament structures need to form an Arg-Glu salt bridge that enables the
329 activation loops to be correctly positioned for catalytic activity (i.e., Arg317-Glu325 in GAC and
330 Arg250-Glu258 in GLS2). This requires a scissor-like movement between two monomers within
331 the same dimer to position their activation loops into close proximity (Figs. 6a, b, insets at the
332 bottom; these movements are indicated by arrows; Extended Data Supplementary movie 1).
333 However, within the GLS2 structure, the ankyrin repeats appear to hinder this movement and
334 thereby may prevent the activation loops from adopting the positions necessary for maximal
335 catalytic capability (Fig. 6b). These effects may help contribute to GLS2 having a lower specific
336 activity compared to GAC.
337
338
339 **DISCUSSION**
340 The glutaminase enzymes GAC and GLS2 have both been implicated in cancer progression
341 due to the upregulation of their expression and catalytic activities[9,10,14,19,20,42]. The elevations in
342 glutamine metabolism triggered by these metabolic enzymes serve to compensate for the
343 uncoupling of glycolysis from the TCA cycle, known as the Warburg effect, by providing the
344 carbon sources necessary for the biosynthetic processes that enable cancer cells to undergo rapid

345 proliferation and survive various types of cellular stress that would otherwise kill normal healthy
346 cells. However, in some cancer contexts, GLS2 has been proposed to function as a tumor
347 suppressor[17,18]. While this raised the question of whether GLS2 might exhibit distinct structural
348 features from GAC, here we show that like GAC, GLS2 assumes a higher order filament-like
349 structure which is directly coupled to catalytic turnover.

350 In our efforts to learn more about the mechanisms by which the glutaminase enzymes catalyze
351 glutamine hydrolysis we had developed fluorescence spectroscopic readouts to monitor directly
352 the binding of the substrate glutamine in the presence and absence of the anionic activator Pi, as
353 well as probe the interactions of allosteric inhibitors while simultaneously assaying enzyme
354 activity[27,37,38,40]. These studies showed how the binding of substrate and anionic activators helped
355 to drive the transition between enzyme dimers to tetramers[25]. Given that the addition of an anionic
356 activator like Pi could induce the formation of glutaminase tetramers and was necessary for
357 enzymatic activity, it was assumed that the dimer-to-tetramer transition was responsible for
358 catalysis. Still, it was puzzling that when comparing the active sites of the dimeric and tetrameric
359 GAC species, there were no apparent differences in the positioning of the key catalytic residues,
360 nor was there any indication of how the activation loops contributed to enzyme activity. However,
361 we have been able to obtain important new insights into the mechanisms of glutaminase activation
362 and catalysis when examining the ability of GAC and GLS2 to form filament-like structures under
363 catalytic conditions, both through the use of cryo-EM and RALS. By performing cryo-EM
364 structural analyses of the GAC (Y466W) mutant which is still able to bind glutamine and Pi but is
365 defective in hydrolysis, we were able to capture a snapshot of the substrate- and activator-induced
366 conformational changes that lead to filament assembly. We found by negative stain EM, cryo-EM,
367 and RALS that the constitutively active GLS2 (K253A) mutant also formed higher-order filament-

368 like structures comprising several enzyme tetramers under catalytic turnover conditions, similar to
369 GAC. Importantly, we demonstrated that the lifetimes of the filament structures for both GAC and
370 GLS2 were directly coupled to catalysis, as they persisted as long as sufficient substrate was
371 available but then rapidly dissociated when the substrate was ultimately used up, confirming
372 suggestions that the formation of glutaminase filaments is directly linked to their catalytic
373 activity[29,31,39].

374 For all prior structures of the glutaminase isozymes, the activation loops were only visible
375 when the enzymes were bound to allosteric inhibitors of the BPTES family of compounds and
376 there were no indications of how they play a critical role in enzyme catalysis, especially given
377 their apparent distance from the active sites. There also was little indication of how the activation
378 loops communicated with the lids that form over the bound substrate, which is necessary for
379 enzyme catalysis[34,38]. However, the cryo-EM structures of activated GAC and GLS2 filaments
380 show activation loops that are well resolved and move toward the active site of each enzyme
381 subunit, positioning an essential tyrosine residue sufficiently close to a catalytically important
382 lysine residue to form a cation-π interaction. This leads to the de-protonation of an active site serine
383 residue, which is then poised for nucleophilic attack on the substrate glutamine. The glutaminase
384 filament structures also show that the lids undergo conformational changes relative to their
385 positions in the apo-enzyme (tetramer), resulting in the insertion of a key tyrosine residue into the
386 active site. These changes effectively close off each active site, locking the substrate glutamine
387 into the proper orientation for catalysis. Several additional hydrogen bonding interactions are
388 evident within the filament structures that help stabilize the interactions between the tetrameric
389 units and enable the activation loops to be inserted into the active sites. Upon catalytic turnover,
390 the release of the product glutamate relieves constraints on the activation loops and introduces

391 flexibility to the lid loops, which disrupts the interface between tetramers and results in the
392 dissociation of the filaments, thus accounting for the tight correlation between enzyme activity and
393 filament formation/dissociation.

394 Our structure-function studies of glutaminase filaments have shed light on how anionic
395 activators like Pi bind to activation loops of the enzymes and drive a dimer-to-tetramer transition
396 and filament assembly which are essential steps for catalysis. They also highlight how allosteric
397 inhibitors targeting the glutaminase enzymes and the presence of ankyrin repeats prevent the
398 activation loops from undergoing the conformational changes necessary for catalytic activity and
399 filament formation. Moreover, these findings now open the way to several interesting new lines of
400 study. For example, new therapeutic strategies might be developed to block the formation of these
401 higher-order oligomers. Identifying other potential activators of both GAC and GLS2 in cancer
402 cells that can induce filament formation will be important, given that the Pi levels necessary to
403 stimulate enzyme activity and filament formation might not be achievable under many
404 physiological contexts. It will also be interesting to see how post-translational modifications such
405 as lysine succinylation, which occur at specific sites on GAC and have been suggested to both
406 promote enzyme activation by stimulating oligomer (tetramer) formation[29] and to enhance
407 ubiquitination and degradation[43], affect filament formation, as well as whether the ankyrin repeats
408 are responsible for conferring GLS2 with functional capabilities distinct from those of GAC in
409 different cancers. Finally, an intriguing possibility will be to see whether the glutaminase enzymes
410 co-assemble in filamentous structures with other enzymes suggested to form higher order
411 oligomers such as glutamate dehydrogenase[28]. Such assemblies might more efficiently couple the
412 activities of members of a metabolic pathway by substrate channeling, with the products of one
413 enzyme being channeled to the next enzyme in the pathway to use as substrates.

414

415

416 **REFERENCES**

417 1. Pavlova, N.N. and C.B. Thompson, *The Emerging Hallmarks of Cancer Metabolism.* Cell
418 Metab, 2016. **23**(1): p. 27-47.

419 2. Faubert, B., A. Solmonson, and R.J. DeBerardinis, *Metabolic reprogramming and cancer*
420 *progression.* Science, 2020. **368**(6487).

421 3. Hanahan, D., *Hallmarks of Cancer: New Dimensions.* Cancer Discov, 2022. **12**(1): p. 31-
422 46.

423 4. Warburg, O., *On the origin of cancer cells.* Science, 1956. **123**(3191): p. 309-14.

424 5. Vander Heiden, M.G., L.C. Cantley, and C.B. Thompson, *Understanding the Warburg*
425 *effect: the metabolic requirements of cell proliferation.* Science, 2009. **324**(5930): p. 1029-
426 33.

427 6. Lukey, M.J., W.P. Katt, and R.A. Cerione, *Targeting amino acid metabolism for cancer*
428 *therapy.* Drug Discov Today, 2017. **22**(5): p. 796-804.

429 7. Yang, C., et al., *Glutamine oxidation maintains the TCA cycle and cell survival during*
430 *impaired mitochondrial pyruvate transport.* Mol Cell, 2014. **56**(3): p. 414-424.

431 8. Leone, R.D., et al., *Glutamine blockade induces divergent metabolic programs to*
432 *overcome tumor immune evasion.* Science, 2019. **366**(6468): p. 1013-1021.

433 9. Lukey, M.J., et al., *Liver-Type Glutaminase GLS2 Is a Druggable Metabolic Node in*
434 *Luminal-Subtype Breast Cancer.* Cell Rep, 2019. **29**(1): p. 76-88 e7.

435 10. Mendez-Lucas, A., et al., *Identifying strategies to target the metabolic flexibility of*
436 *tumours.* Nat Metab, 2020. **2**(4): p. 335-350.

437 11. Altman, B.J., Z.E. Stine, and C.V. Dang, *From Krebs to clinic: glutamine metabolism to*
438 *cancer therapy.* Nat Rev Cancer, 2016. **16**(11): p. 749.
439 12. Harding, J.J., et al., *A Phase I Dose-Escalation and Expansion Study of Telaglenastat in*
440 *Patients with Advanced or Metastatic Solid Tumors.* Clin Cancer Res, 2021. **27**(18): p.
441 4994-5003.
442 13. Shen, Y.A., et al., *Inhibition of glutaminolysis in combination with other therapies to*
443 *improve cancer treatment.* Curr Opin Chem Biol, 2021. **62**: p. 64-81.
444 14. Wang, J.B., et al., *Targeting mitochondrial glutaminase activity inhibits oncogenic*
445 *transformation.* Cancer Cell, 2010. **18**(3): p. 207-19.
446 15. Katt, W.P., et al., *Dibenzophenanthridines as inhibitors of glutaminase C and cancer cell*
447 *proliferation.* Mol Cancer Ther, 2012. **11**(6): p. 1269-78.
448 16. Byun, J.K., et al., *Inhibition of Glutamine Utilization Synergizes with Immune Checkpoint*
449 *Inhibitor to Promote Antitumor Immunity.* Mol Cell, 2020. **80**(4): p. 592-606 e8.
450 17. Zhang, C., et al., *Glutaminase 2 is a novel negative regulator of small GTPase Rac1 and*
451 *mediates p53 function in suppressing metastasis.* Elife, 2016. **5**: p. e10727.
452 18. Suzuki, S., et al., *GLS2 Is a Tumor Suppressor and a Regulator of Ferroptosis in*
453 *Hepatocellular Carcinoma.* Cancer Res, 2022. **82**(18): p. 3209-3222.
454 19. Dias, M.M., et al., *GLS2 is protumorigenic in breast cancers.* Oncogene, 2020. **39**(3): p.
455 690-702.
456 20. Saha, S.K., et al., *Multiomics Analysis Reveals that GLS and GLS2 Differentially Modulate*
457 *the Clinical Outcomes of Cancer.* J Clin Med, 2019. **8**(3).
458 21. Katt, W.P., M.J. Lukey, and R.A. Cerione, *A tale of two glutaminases: homologous*
459 *enzymes with distinct roles in tumorigenesis.* Future Med Chem, 2017. **9**(2): p. 223-243.

460 22. Ferreira, I.M., et al., *Structure and activation mechanism of the human liver-type*
461 *glutaminase GLS2.* Biochimie, 2021. **185**: p. 96-104.
462 23. Nguyen, T.T., W.P. Katt, and R.A. Cerione, *Alone and together: current approaches to*
463 *targeting glutaminase enzymes as part of anti-cancer therapies.* Future Drug Discov, 2023.
464 **4**(4): p. FDD79.
465 24. DeLaBarre, B., et al., *Full-length human glutaminase in complex with an allosteric*
466 *inhibitor.* Biochemistry, 2011. **50**(50): p. 10764-70.
467 25. Nguyen, T.T., et al., *High-resolution structures of mitochondrial glutaminase C tetramers*
468 *indicate conformational changes upon phosphate binding.* J Biol Chem, 2022. **298**(2): p.
469 101564.
470 26. Gross, M.I., et al., *Antitumor activity of the glutaminase inhibitor CB-839 in triple-negative*
471 *breast cancer.* Mol Cancer Ther, 2014. **13**(4): p. 890-901.
472 27. Milano, S.K., et al., *New insights into the molecular mechanisms of glutaminase C*
473 *inhibitors in cancer cells using serial room temperature crystallography.* J Biol Chem,
474 2022. **298**(2): p. 101535.
475 28. Park, C.K. and N.C. Horton, *Structures, functions, and mechanisms of filament forming*
476 *enzymes: a renaissance of enzyme filamentation.* Biophys Rev, 2019. **11**(6): p. 927-994.
477 29. Jiang, B., et al., *Filamentous GLS1 promotes ROS-induced apoptosis upon glutamine*
478 *deprivation via insufficient asparagine synthesis.* Mol Cell, 2022. **82**(10): p. 1821-1835 e6.
479 30. Cassago, A., et al., *Mitochondrial localization and structure-based phosphate activation*
480 *mechanism of Glutaminase C with implications for cancer metabolism.* Proc Natl Acad Sci
481 U S A, 2012. **109**(4): p. 1092-7.

482 31. Ferreira, A.P., et al., *Active glutaminase C self-assembles into a supratetrameric oligomer*
483 *that can be disrupted by an allosteric inhibitor.* J Biol Chem, 2013. **288**(39): p. 28009-20.
484 32. Li, J., A. Mahajan, and M.D. Tsai, *Ankyrin repeat: a unique motif mediating protein-*
485 *protein interactions.* Biochemistry, 2006. **45**(51): p. 15168-78.
486 33. Pasquali, C.C., et al., *The origin and evolution of human glutaminases and their atypical*
487 *C-terminal ankyrin repeats.* J Biol Chem, 2017. **292**(27): p. 11572-11585.
488 34. Li, Y., et al., *The activation loop and substrate-binding cleft of glutaminase C are*
489 *allosterically coupled.* J Biol Chem, 2020. **295**(5): p. 1328-1337.
490 35. Robinson, M.M., et al., *Novel mechanism of inhibition of rat kidney-type glutaminase by*
491 *bis-2-(5-phenylacetamido-1,2,4-thiadiazol-2-yl)ethyl sulfide (BPTES).* Biochem J, 2007.
492 **406**(3): p. 407-14.
493 36. Huang, Q., et al., *Characterization of the interactions of potent allosteric inhibitors with*
494 *glutaminase C, a key enzyme in cancer cell glutamine metabolism.* J Biol Chem, 2018.
495 **293**(10): p. 3535-3545.
496 37. Stalnecker, C.A., et al., *Mechanism by which a recently discovered allosteric inhibitor*
497 *blocks glutamine metabolism in transformed cells.* Proc Natl Acad Sci U S A, 2015. **112**(2):
498 p. 394-9.
499 38. Li, Y., et al., *Mechanistic Basis of Glutaminase Activation: A KEY ENZYME THAT*
500 *PROMOTES GLUTAMINE METABOLISM IN CANCER CELLS.* J Biol Chem, 2016.
501 **291**(40): p. 20900-20910.
502 39. Moller, M., et al., *Small angle X-ray scattering studies of mitochondrial glutaminase C*
503 *reveal extended flexible regions, and link oligomeric state with enzyme activity.* PLoS One,
504 2013. **8**(9): p. e74783.

505 40. Stalnecker, C.A., J.W. Erickson, and R.A. Cerione, *Conformational changes in the*
506 *activation loop of mitochondrial glutaminase C: A direct fluorescence readout that*
507 *distinguishes the binding of allosteric inhibitors from activators.* J Biol Chem, 2017.
508 **292**(15): p. 6095-6107.
509 41. Brown, G., et al., *Functional and structural characterization of four glutaminases from*
510 *Escherichia coli and Bacillus subtilis.* Biochemistry, 2008. **47**(21): p. 5724-35.
511 42. Gao, P., et al., *c-Myc suppression of miR-23a/b enhances mitochondrial glutaminase*
512 *expression and glutamine metabolism.* Nature, 2009. **458**(7239): p. 762-5.
513 43. Greene, K.S., et al., *SIRT5 stabilizes mitochondrial glutaminase and supports breast*
514 *cancer tumorigenesis.* Proc Natl Acad Sci U S A, 2019.

515 **METHODS**

516 **Recombinant glutaminase expression and purification**

517 An N-terminal His-tagged form of the full-length human liver-type glutaminase isoform GLS2
518 without the mitochondrial localization sequence (residue 38-602) was cloned into the pET28a
519 plasmid as previously described[36]. Site-directed mutagenesis was performed using Phusion DNA
520 polymerase (New England Biolabs, NEB). Protein expression was carried out first by transforming
521 constructs into *E. Coli* BL21 (DE3) competent cells (NEB), which were then grown in LB media
522 overnight with 50 μg/mL kanamycin. The starter cultures were subsequently inoculated at ~1:100
523 ratio in 6 L cultures with the same antibiotic concentration and left shaking at 37°C, 180 rpm for
524 3-4 hours until the OD600 reached between 0.6 and 0.8. The flasks were then chilled at 4°C for 1-
525 2 hours before induction with 30 μM IPTG (isopropyl β-D-1-thiogalactopyranoside) and shaking
526 at room temperature (RT), 180 rpm for 16-18 hours. Cells were collected by centrifugation at
527 5,000xg for 10 minutes and frozen before resuspension in 150 mL lysis buffer (50 mM Tris-HCl
528 pH 8.5, 500 mM NaCl, 10% glycerol), supplemented with protease inhibitor cocktail (Roche).
529 Cells were lysed with lysozyme and mechanical sonication, and DNase I was added to reduce the
530 mixture's viscosity. The soluble fractions were separated from the debris by ultra-centrifugation
531 (Ti45 rotor, 40,000 rpm for 45 minutes). The lysate was then loaded onto Co^{2+}-charged TALON
532 resin (GoldBio), equilibrated previously with the wash buffer (50 mM Tris-HCl pH 8.5, 10 mM
533 NaCl, 10 mM imidazole). The protein that bound to the column was washed with the wash buffer
534 and eluted with wash buffer supplemented with 320 mM imidazole. Further purification was
535 performed by anion exchange chromatography using HiTrap Q HP column (Cytiva) and size-
536 exclusion chromatography using Superdex 200 pg 16/600 column (GE Healthcare). Human GAC
537 preparations were prepared as previously described[25,27]. Proteins were kept in 20 mM Tris-HCl pH

538 8.5, 150 mM NaCl, snap-frozen in liquid nitrogen, and stored at -80°C. Protein concentrations
539 were determined by absorbance at 280 nm using extinction coefficients calculated using the
540 Expasy ProtParam tool.
541
542 **Right-angle light scattering (RALS)**
543 Frozen glutaminase aliquots were thawed on ice and diluted to a final concentration of 2 μM
544 in 1 mL of gel filtration buffer (20 mM Tris-HCl pH 8.5, 150 mM NaCl) added in a 1.2 mL cuvette
545 and inserted into a Varian Cary Eclipse fluorimeter. The cuvette temperature was set to 25°C and
546 stirred with a magnetic stir bar. The signal was recorded using excitation and emission wavelengths
547 of 340 nm (5 nm bandpass). The samples were incubated until the signal was stable (~2-3 mins),
548 then 100 μL of glutamine from a 200 mM stock solution were added to initiate the reaction.
549 Subsequently, 100 μL of inorganic phosphate (1 M) or glutamate (200 mM) were added for further
550 analysis. The raw scattering traces were filtered to improve the signal-to-noise ratio using SciPy
551 (version 1.9.2) and plotted using Matplotlib (version 3.7.1).
552
553 **Negative stain Electron Microscopy**
554 Formvar/carbon film 200 mesh copper grids (Electron Microscopy Sciences, EMS) were
555 plasma cleaned by using PELCO easiGlow system (TED PELLA). Glutaminase (final
556 concentration: 1 μM) was mixed with the substrate glutamine (final concentration: 20 mM).
557 Inorganic phosphate (K_2HPO_4 final concentration: 50 mM) was added to the mixture when needed.
558 The mixture was incubated at RT for 30 seconds. Then, 10 μL of the mixture was applied onto the
559 grids for a 60-second incubation, and the excess protein solution was blotted with filter paper. Ten
560 μL of 2% uranyl acetate were then applied to the grid twice for two 30-second stainings followed

561 by blotting. The grids were air-dried for 5 minutes and visualized by Thermo Fischer F200Ci
562 electron microscope at 120 keV.
563
564 **Cryo-EM grids preparation and images acquisition for apo-GLS2**
565 Four μL of 5 μM GLS2 were applied to plasma-cleaned grids (300 mesh UltraAu Foil
566 R1.2/1.3, Electron Microscopy Sciences, EMS) for a 30-second incubation. The excess solution
567 was blotted for 4-6 seconds with filter paper by a Vitrobot mark IV (Thermo Fischer Scientific).
568 Grids were subsequently vitrified in liquid ethane and stored in liquid nitrogen. Cryo-EM single
569 particle micrographs of apo-GLS2 were collected on a Talos Arctica (Thermo Fischer Scientific)
570 at the Cornell Center for Materials Research. The microscope was operated at 200 keV at 63,000x
571 nominal magnification using a Gatan K3 direct electron camera in super-resolution mode, with a
572 Gatan GIF Quantum LS Imaging energy filter, corresponding to a physical pixel size of 1.23 Å/pix.
573 Given the orientation bias of the sample, a non-tilted dataset of 1,171 images and a 30-degree tilted
574 dataset of 488 images were collected and merged for further data processing. The images were
575 obtained with a defocus range of -0.8 to -2.0 um by EPU (Thermo Fischer Scientific). Each stack
576 movie was recorded with 50 frames for a total dose of ~50 e-/Å^2.
577
578 **Cryo-EM grids preparation and images acquisition for GLS2 (K253A) filament**
579 Human GLS2 (K253A), 3 μM, was mixed with 20 mM glutamine to initiate filament
580 formation. The mixture was applied to plasma-cleaned grids (300 mesh Quantifoil Au R1.2/1.3,
581 EMS) for 30-second incubations. The excess solution was blotted for 5-7 seconds with filter paper
582 by a Vitrobot mark IV. Grids were subsequently vitrified in liquid ethane and stored in liquid
583 nitrogen. Cryo-EM single particle micrographs of apo-GLS2 were collected on a Titan Krios

584 (Thermo Fischer Scientific) at The New York Structural Biology Center. The microscope was
585 operated at 300 keV at 81,000x nominal magnification using a Gatan K3 direct electron camera in
586 counting mode, corresponding to a physical pixel size of 1.058 Å/pix. Thirty-eight hundred and
587 four images were obtained with a defocus range of -0.8 to -2.0 mm by Leginon[44]. Each stack movie
588 was recorded with 40 frames for a total dose of ~50 e-/Å^2.
589

590 **Cryo-EM grids preparation and images acquisition for GAC (Y466W) filament**

591 Human GAC (Y466W), 8 μM, was mixed with 20 mM glutamine and 1M inorganic phosphate
592 to initiate filament formation. The mixture was applied to plasma-cleaned grids (300 mesh
593 Quantifoil Cu R1.2/1.3, EMS) for 30-second incubations. The excess solution was blotted for 2-3
594 seconds with filter paper by a Vitrobot mark IV. Grids were subsequently vitrified in liquid ethane
595 and stored in liquid nitrogen. Cryo-EM single particle micrographs of GAC (Y466W) filament
596 were collected on a Talos Arctica (Thermo Fischer Scientific) at the Cornell Center for Materials
597 Research. The microscope was operated at 200 keV at 63,000x nominal magnification using a
598 Gatan K3 direct electron camera in counted mode, with a Gatan GIF Quantum LS Imaging energy
599 filter, corresponding to a physical pixel size of 1.31 Å/pix. Thirty-nine hundred images were
600 obtained with a defocus range of -0.8 to -2.0 mm by SerialEM[45]. Each stack movie was recorded
601 with 50 frames for a total dose of ~50 e-/Å^2.
602

603 **Cryo-EM data processing**

604 For the apo-GLS2 map, dose-fractionated image stacks were subjected to motioncor2 wrapped
605 in RELION 4.0.0.[46-48] through SBGrid, followed by patch CTF estimation in CryoSPARC
606 V4.0.0.[49]. The motion-corrected micrographs with CTF better than 4 Å were passed for later

607 processing. A blob picker in CryoSPARC was used to generate the templates for further Topaz
608 picking[50], where ~1M particles were picked. The particles were subjected to 3D classification and
609 heterogenous refinement, and only the best classes were kept. The remaining ~329K particles were
610 subjected to homogenous and heterogenous refinement. The final reconstruction with C2
611 symmetry yields a map with a resolution of 3.12 Å determined by FSC. The workflow is provided
612 in Extended Data Fig. 8. Cryo-EM maps are visualized in ChimeraX[51].

613 For the GAC (Y466W) filament structure, dose-fractionated image stacks were subjected to
614 patch motion correction, followed by patch CTF estimation in CryoSPARC V4.2.1. The motion-
615 corrected micrographs with CTF better than 4 Å were passed for later processing. The template-
616 free filament trace job in CryoSPARC picks ~397K particles for 2D classification. About 180K
617 particles were extracted and subjected to 3D classification. The best ~45k particles were
618 reconstructed with C2 symmetry and refined to yield a 3.35 Å map determined by FSC. The
619 workflow is provided in Extended Data Fig 9.

620 For the GLS2 (K253A) filament structure, dose-fractionated image stacks were subjected to
621 patch motion correction, followed by patch CTF estimation in CryoSPARC V4.0.0. The motion-
622 corrected micrographs with CTF better than 4 Å were passed for later processing, which yielded
623 3,640 micrographs. Manual picking in CryoSPARC was used on 40 micrographs to pick ~600
624 particles manually, which yielded five classes of templates by 2D classification. The selected
625 template was used for the filament trace job in CryoSPARC to template pick particles. About 333K
626 particles were extracted and subjected to 3D classification. The best ~48k particles were
627 reconstructed and refined to yield a 3.3 Å map determined by FSC. The workflow is provided in
628 Extended Data Fig 10.

629

630 **Model building and refinement**

631 The initial apo-GLS2, GAC (Y466W), and GLS2 (K253A) model was adapted from the PDB
632 entry 4BQM for the catalytic domain and 5U0K for the ankyrin repeats. First, all models were
633 manually docked into the map by UCSF ChimeraX. Next, the model was fitted into the map by
634 ISOLDE for the overall adjustment[52], then underwent multiple rounds of automatic refinement
635 using Phenix real space refinement[53], and manual adjusting and building ligands using Coot[54].
636 Finally, validation was performed with MolProbity[55]. The final refinement statistics is provided in
637 Extended Data Table 1.

638

639 **Data availability**

640 The cryo-EM density maps and the atomic model for apo-GLS2, GAC (Y466W) and the
641 GLS2 (K253A) filament structure reported in this paper have been deposited in EM Data Bank
642 (EMDB: EMD-40920, EMD-40918, and EMD-40950) and the Protein Data Bank (PDB: 8SZL,
643 8SZJ, and 8T0Z), respectively.

644

645 **Code availability**

646 No custom computer code was used in this study.

647

648 44. Suloway, C., et al., *Automated molecular microscopy: the new Leginon system.* J Struct
649 Biol, 2005. 151(1): p. 41-60.
650 45. Mastronarde, D.N., *Automated electron microscope tomography using robust prediction*
651 *of specimen movements.* J Struct Biol, 2005. **152**(1): p. 36-51.
652 46. Morin, A., et al., *Collaboration gets the most out of software.* Elife, 2013. **2**: p. e01456.

653 47. Scheres, S.H., *RELION: implementation of a Bayesian approach to cryo-EM structure*
654 *determination.* J Struct Biol, 2012. **180**(3): p. 519-30.
655 48. Zheng, S.Q., et al., *MotionCor2: anisotropic correction of beam-induced motion for*
656 *improved cryo-electron microscopy.* Nat Methods, 2017. **14**(4): p. 331-332.
657 49. Punjani, A., et al., *cryoSPARC: algorithms for rapid unsupervised cryo-EM structure*
658 *determination.* Nat Methods, 2017. **14**(3): p. 290-296.
659 50. Bepler, T., et al., *Positive-unlabeled convolutional neural networks for particle picking in*
660 *cryo-electron micrographs.* Nat Methods, 2019. **16**(11): p. 1153-1160.
661 51. Pettersen, E.F., et al., *UCSF ChimeraX: Structure visualization for researchers, educators,*
662 *and developers.* Protein Sci, 2021. **30**(1): p. 70-82.
663 52. Croll, T.I., *ISOLDE: a physically realistic environment for model building into low-*
664 *resolution electron-density maps.* Acta Crystallogr D Struct Biol, 2018. **74**(Pt 6): p. 519-
665 530.
666 53. Liebschner, D., et al., *Macromolecular structure determination using X-rays, neutrons and*
667 *electrons: recent developments in Phenix.* Acta Crystallogr D Struct Biol, 2019. **75**(Pt 10):
668 p. 861-877.
669 54. Emsley, P., et al., *Features and development of Coot.* Acta Crystallogr D Biol Crystallogr,
670 2010. **66**(Pt 4): p. 486-501.
671 55. Williams, C.J., et al., *MolProbity: More and better reference data for improved all-atom*
672 *structure validation.* Protein Sci, 2018. **27**(1): p. 293-315.

673

674

675 **Acknowledgments** We thank Drs. Katherine Spoth, Mariena Silvestry-Ramos, Kasahun Neselu,
676 and Edward Eng for help with EM instrumentation. We would also like to thank Drs. Brian R.
677 Crane and Sekar Ramachandran for the helpful feedback on the structural analysis, and Samuel L.
678 Deck and Megan Xu for helping produce glutaminase mutants. This work was supported by grants
679 from the NIH (R35GM122575 and R01CA201402). The acquisition of the human apo-GLS2 and
680 mouse GAC (Y466W) structures used the Cornell Center for Materials Research Shared Facilities,
681 which is supported by NSF (DMR- 1719875). The collection of negative stain images relied on
682 using an instrument supported by the NIH through award S10OD030470-01. The acquisition of
683 the GLS2 (K253A) structure was performed at the National Center for CryoEM Access and
684 Training (NCCAT) and the Simons Electron Microscopy Center located at the New York
685 Structural Biology Center, supported by the NIH Common Fund Transformative High-Resolution
686 Cryo-Electron Microscopy program (U24 GM129539) and by grants from the Simons Foundation
687 (SF349247) and NY State Assembly.

688

689 **Author Contributions** All authors contributed to each aspect of the study, but primarily, T-
690 T.T.N., S.K.M, C.A. and S.F. developed methods to express and purify the glutaminase and
691 mutants; C.A. and S.F. developed and performed the RALS assay; S.F. performed the activity
692 assay; S.F. prepared the samples for negative stain EM and cryo-EM, and collected and processed
693 the EM data. S.F. built the apo-GLS2, GAC Y466W filament and GLS2 K253A filament
694 structures; S.F., C.A., T-T.T.N., S.K.M. and R.A.C. analysed the structures; S.F., C.A., T-T.T.N.,
695 S.K.M. and R.A.C. wrote the manuscript; R.A.C. conceived of and oversaw the project.

696

697 **Competing interests** The authors declare no competing interests.

Additional information

Supplementary information is available for the paper.

Correspondence and requests for materials should be addressed to Richard A. Cerione.

Reprints and permissions information is available at www.nature.com/reprints.

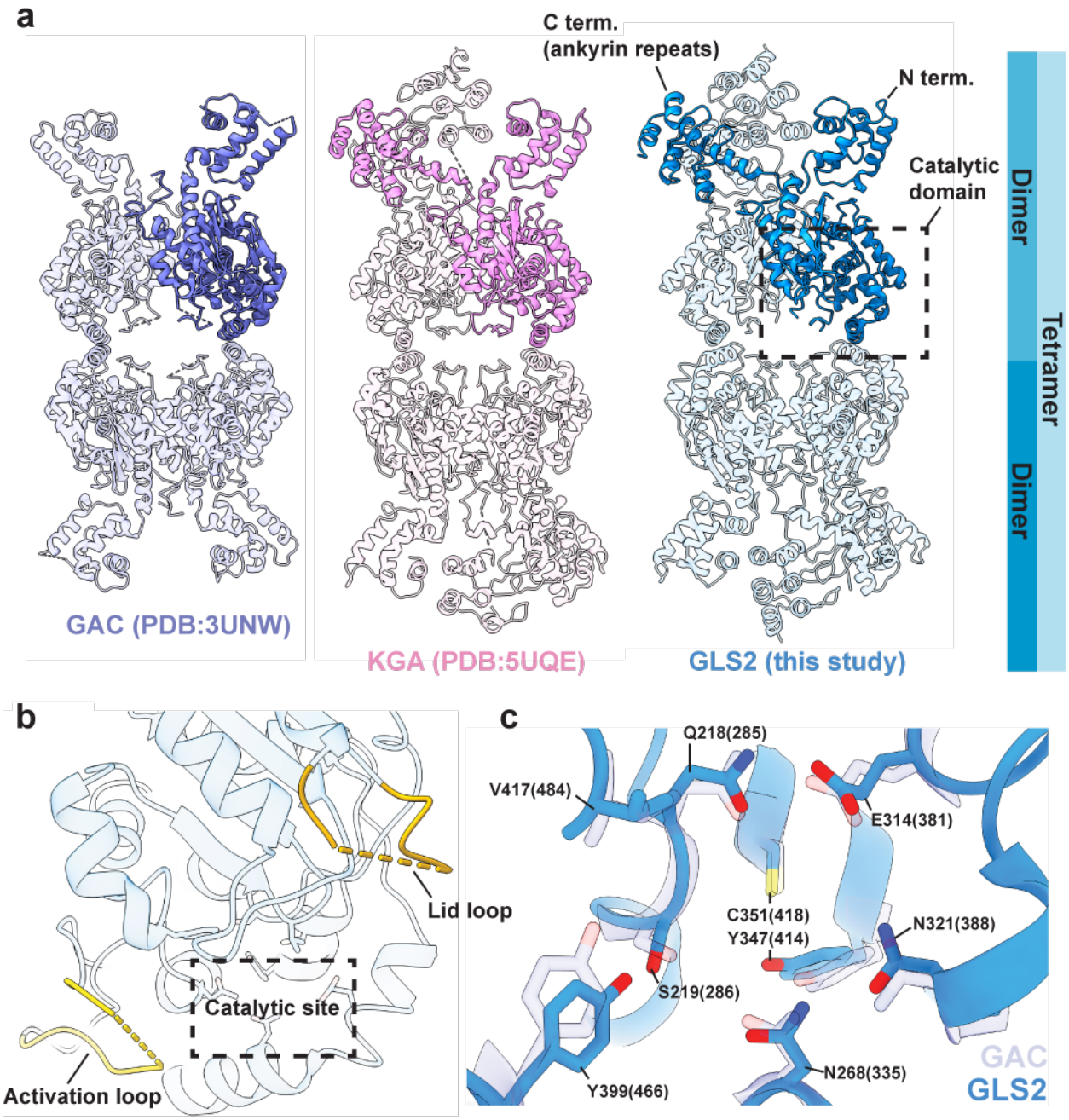
a
C term.
(ankyrin repeats)
N term.
Catalytic
domain
Dimer
Tetramer
Dimer
GAC (PDB:3UNW)
KGA (PDB:5UQE)
GLS2 (this study)
b
Lid loop
Catalytic site
Activation loop
c
Q218(285)
V417(484)
E314(381)
C351(418)
Y347(414)
N321(388)
S219(286)
N268(335)
Y399(466)
GAC
GLS2

704

705

706 **Figure 1. The cryo-EM structure of human full-length apo-GLS2 and its comparison with**
707 **the X-ray crystal structures of the GLS isoforms.**
708 **(a)** The structures of tetrameric GAC, KGA, and GLS2 (from left to right). One monomer in each
709 tetramer is highlighted in solid color. The glutaminase catalytic domain (dashed box in (A)). **(b)**
710 Zoomed in view of the catalytic domain showing the activation loop (light yellow), the catalytic
711 site (dashed box) and the lid loop (dark yellow). **(c)** The conserved catalytic residues of GLS2
712 (blue) and GAC (PDB ID: 3UNW, light purple). Residues are numbered according to human
713 GLS2 and GAC numbering is shown in parentheses.
714

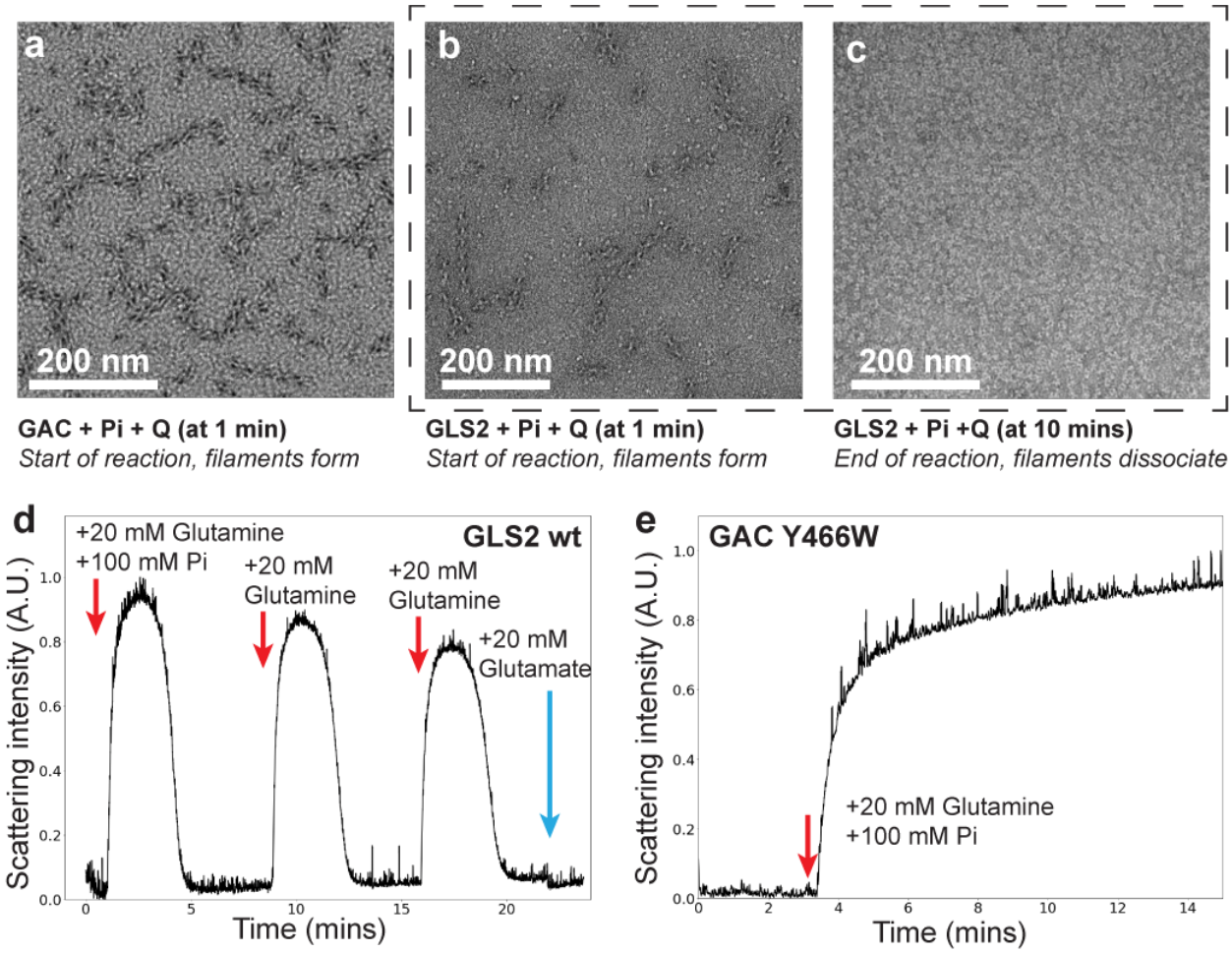
a
200 nm
b
200 nm
c
200 nm
GAC + Pi + Q (at 1 min)
Start of reaction, filaments form
GLS2 + Pi + Q (at 1 min)
Start of reaction, filaments form
GLS2 + Pi +Q (at 10 mins)
End of reaction, filaments dissociate
d
GLS2 wt
+20 mM Glutamine
+100 mM Pi
+20 mM Glutamine
+20 mM Glutamine
+20 mM Glutamate
Scattering intensity (A.U.)
Time (mins)
e
GAC Y466W
+20 mM Glutamine
+100 mM Pi
Scattering intensity (A.U.)
Time (mins)

715

716

717 **Figure 2. The formation of the glutaminase filaments is directly coupled to catalytic**
718 **activity.**
719 **(a)** Negative stain EM of GAC (1 μM) with inorganic phosphate (Pi, 100 mM) one minute after
720 adding glutamine (Q, 20 mM). **(b)** Negative stain EM of GLS2 (1 μM) with Pi (100 mM) one
721 minute after adding glutamine (20 mM). **(c)** Negative stain EM of GLS2 (1 μM) with Pi (100
722 mM) 10 minutes after adding glutamine (20 mM). **(d)** Right-angle light scattering (RALS) of
723 GLS2 (2 μM) with Pi (100 mM) after subsequent additions of glutamine (20 mM), or glutamate
724 (20 mM). **(e)** RALS of GAC (Y466W) with Pi (100 mM) and glutamine (20 mM).

725

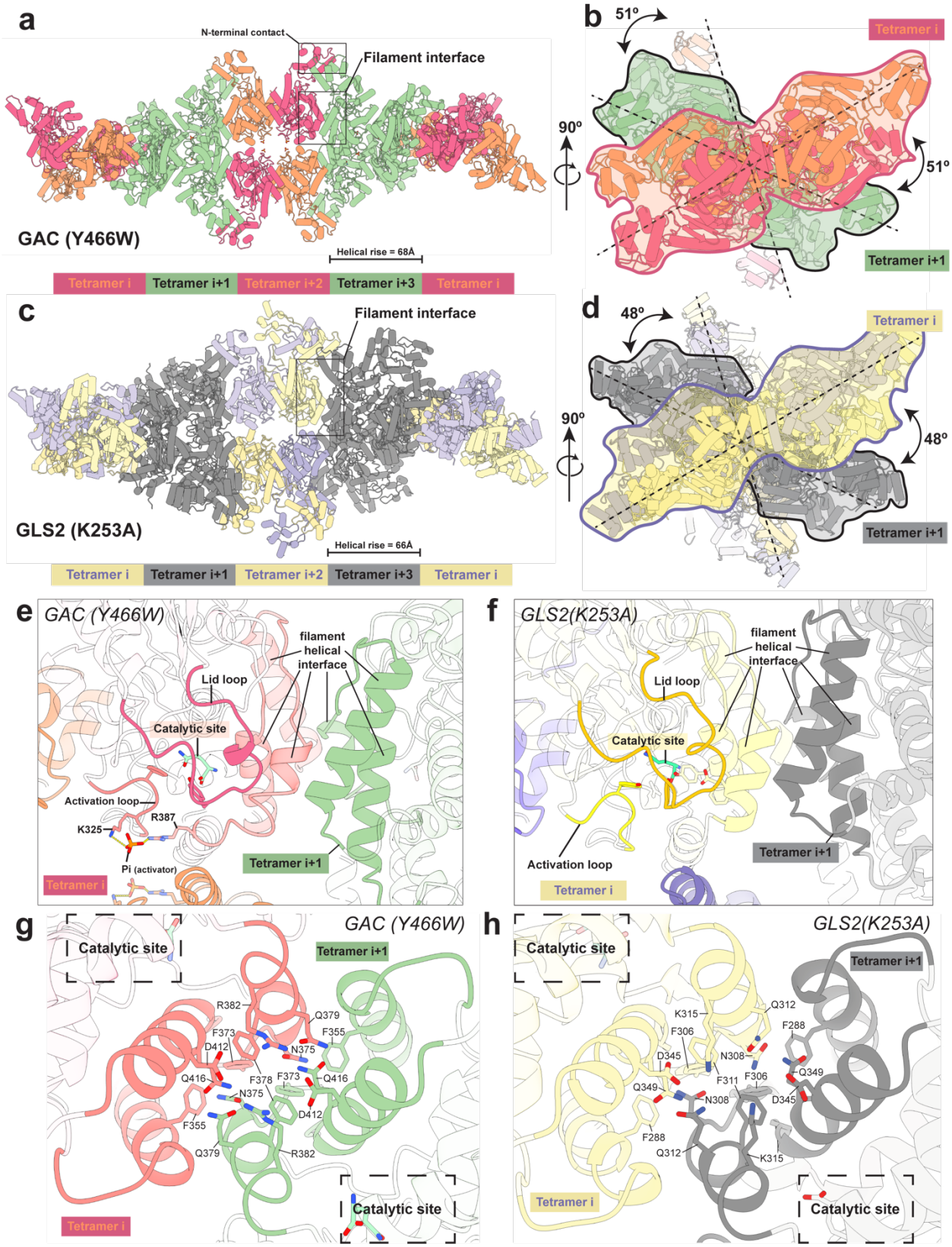
a
N-terminal contact
Filament interface
GAC (Y466W)
Helical rise = 68Å
Tetramer i
Tetramer i+1
Tetramer i+2
Tetramer i+3
Tetramer i
b
51°
Tetramer i
90°
51°
Tetramer i+1
c
Filament interface
GLS2 (K253A)
Helical rise = 66Å
Tetramer i
Tetramer i+1
Tetramer i+2
Tetramer i+3
Tetramer i
d
48°
Tetramer i
90°
48°
Tetramer i+1
e
GAC (Y466W)
filament
helical
interface
Lid loop
Catalytic site
Activation loop
K325
R387
Pi (activator)
Tetramer i+1
Tetramer i
f
GLS2(K253A)
filament
helical
interface
Lid loop
Catalytic site
Activation loop
Tetramer i+1
Tetramer i
g
GAC (Y466W)
Catalytic site
Tetramer i+1
R382
Q379
F373
F355
D412
N375
Q416
F378
F373
Q416
N375
D412
F355
Q379
R382
Catalytic site
Tetramer i
h
GLS2(K253A)
Catalytic site
Tetramer i+1
K315
Q312
F306
F288
D345
N308
F311
F306
Q349
Q349
N308
D345
F288
Q312
K315
Tetramer i
Catalytic site

726

727 **Figure 3. Structures of the human GAC (Y466W) filament and the human GLS2 (K253A)**
728 **filament captured under catalytic turnover conditions.**
729 **(a)** Structure of the GAC (Y466W) filament showing a five tetramer stretch of the higher-order
730 oligomer with a helical rise of 68 Å. Tetramers are colored alternately either orange and red or
731 green. The orange and red tetramers are colored to distinguish between monomers in each tetramer.
732 The filament interface and the N-terminal contacts are highlighted. **(b)** The GAC (Y466W)
733 filament viewed down the filament axis. The first two tetramers are outlined with red and black
734 silhouettes, sequentially. The dashed line indicates the longest dimension of each tetramer and the
735 51° rotation around the filament axis between tetramers. **(c)** Structure of the GLS2 (K253A)
736 filament showing a five tetramer stretch of the higher-order oligomer with a helical rise of 66 Å.
737 Tetramers are colored alternately either purple and yellow or gray. The purple and yellow tetramers
738 are colored to distinguish between monomers in each tetramer. The filament interface is
739 highlighted. **(d)** The GLS2 (K253A) filament viewed down the filament axis. The first two
740 tetramers are outlined with purple and black silhouettes, sequentially. The dashed line indicates
741 the longest dimension of each tetramer and the 48° rotation around the filament axis between
742 tetramers. **(e-f)** The position of the helical filament interface, the activation loop, the catalytic site,
743 and the lid loop in GAC (**e**, red) and GLS2 (**f**, yellow). The next tetramer in the filament is colored
744 green in GAC and gray in GLS2. The helical filament interface is shown in solid colors. **(g-h)** The
745 interaction network at the helical filament interface between tetramers for GAC (**g**, red and green)
746 and GLS2 (**h**, yellow and gray). The close proximity of the catalytic site to the helical filament
747 interface is highlighted with a dashed box.

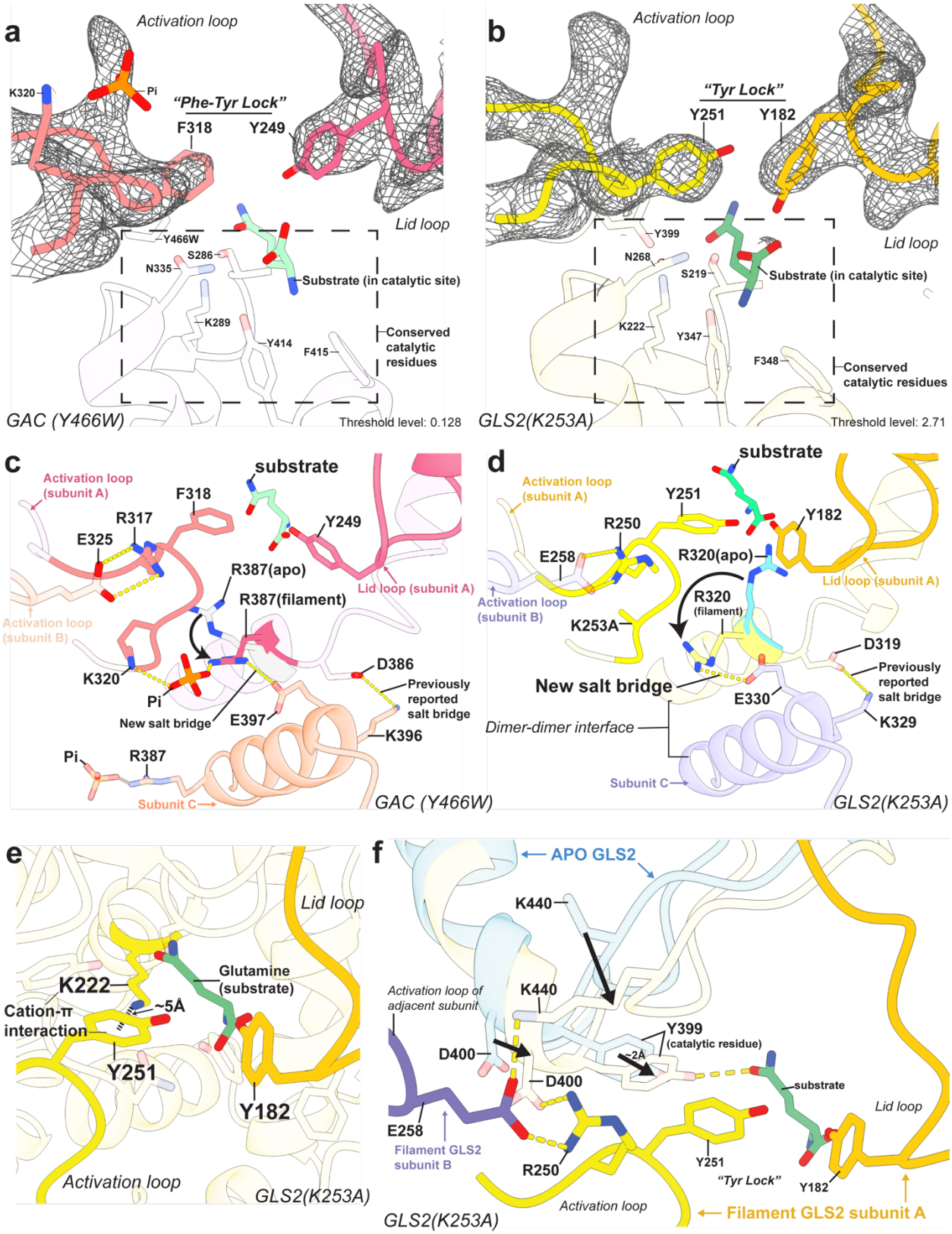
a
Activation loop
K320
Pi
"Phe-Tyr Lock"
F318
Y249
Lid loop
Y466W
S286
N335
Substrate (in catalytic site)
K289
Y414
F415
Conserved catalytic residues
GAC (Y466W)
Threshold level: 0.128
b
Activation loop
"Tyr Lock"
Y251
Y182
Y399
N268
S219
Lid loop
Substrate (in catalytic site)
K222
Y347
F348
Conserved catalytic residues
GLS2(K253A)
Threshold level: 2.71
c
Activation loop (subunit A)
substrate
F318
R317
Y249
E325
R387(apo)
Lid loop (subunit A)
R387(filament)
Activation loop (subunit B)
K320
D386
Pi
Previously reported salt bridge
New salt bridge
E397
K396
Pi
R387
Subunit C
GAC (Y466W)
d
substrate
Activation loop (subunit A)
Y251
R250
Y182
E258
R320(apo)
Lid loop (subunit A)
Activation loop (subunit B)
R320 (filament)
K253A
D319
New salt bridge
Previously reported salt bridge
E330
K329
Dimer-dimer interface
Subunit C
GLS2(K253A)
e
Lid loop
Glutamine (substrate)
K222
Cation-π interaction
~5Å
Y251
Y182
Activation loop
GLS2(K253A)
f
APO GLS2
K440
Activation loop of adjacent subunit
K440
Y399 (catalytic residue)
D400
~2Å
D400
substrate
Lid loop
E258
Filament GLS2 subunit B
R250
Y251
"Tyr Lock"
Y182
Activation loop
Filament GLS2 subunit A
GLS2(K253A)

748

749

750 **Figure 4. Structures of the GAC and GLS2 filaments reveal allosteric conformational**
751 **changes within the glutaminase tetrameric units during catalysis.**
752 **(a-b)** The phenylalanine-tyrosine lock in GAC (Phe318 and Tyr249) and the tyrosine lock in GLS2
753 (Tyr251 and Tyr182). Conserved catalytic residues are labeled, and the electron densities of the
754 activation loop and the lid loop are shown as mesh. **(c)** The movement of Arg387 between apo-
755 GAC (PDB ID: 3UNW, Arg387 is shown in light gray) and the GAC (Y466W) filament (pink) is
756 shown with an arrow. The interactions between inorganic phosphate (Pi) and residues Lys320 and
757 Arg387 near the activation loop in the GAC (Y466W) filament are highlighted. Salt bridges
758 between GAC dimers within a tetramer (pink and salmon) are labeled as dashed yellow lines. **(d)**
759 The movement of Arg320 between apo-GLS2 (Arg320 is shown in cyan) and the GLS2 (K253A)
760 filament (yellow) is shown with an arrow. Salt bridges between GLS2 dimers within a tetramer
761 (yellow and purple) are labeled as dashed yellow lines. **(e)** The tyrosine lock in GLS2 consists of
762 Tyr251 from the activation loop (yellow) and Tyr182 from the lid loop (orange). Glutamine is
763 shown in green and the cation-π interaction between Lys222 and Tyr251 is labeled. **(f)** The
764 movement of conserved catalytic residue Tyr399 between apo-GLS2 (light blue) and the GLS2
765 filament (light yellow) is shown with an arrow. The activation loops of two adjacent monomers
766 within the GLS2 filament are colored yellow (subunit A) and purple (subunit B). Interactions
767 between key residues consisting of hydrogen bonds and salt bridges are shown as yellow dashed
768 lines.

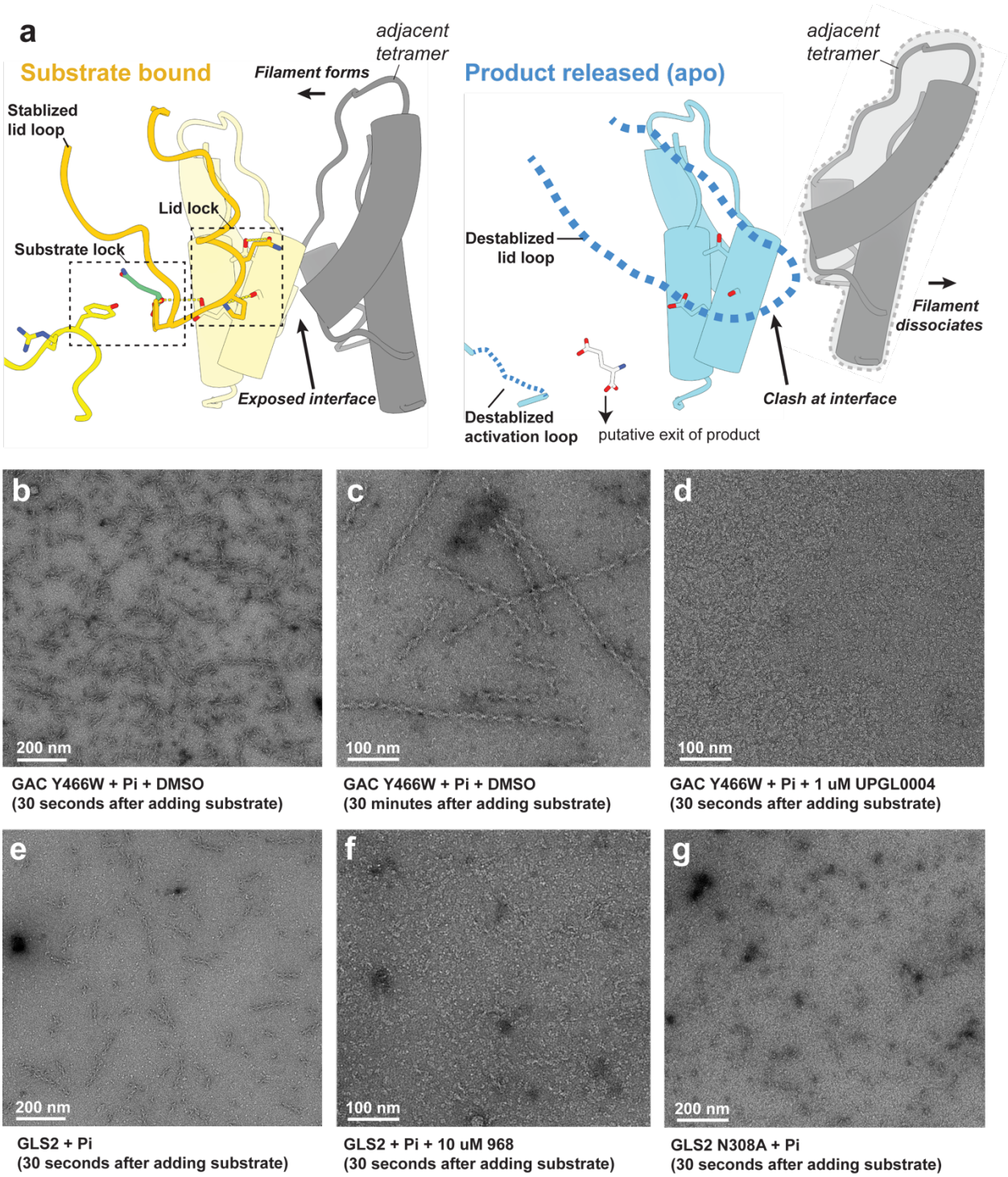
a
Substrate bound
Filament forms
adjacent tetramer
Stablized lid loop
Lid lock
Substrate lock
Exposed interface
Product released (apo)
adjacent tetramer
Destablized lid loop
Filament dissociates
Clash at interface
Destablized activation loop
putative exit of product
b
200 nm
GAC Y466W + Pi + DMSO
(30 seconds after adding substrate)
c
100 nm
GAC Y466W + Pi + DMSO
(30 minutes after adding substrate)
d
100 nm
GAC Y466W + Pi + 1 uM UPGL0004
(30 seconds after adding substrate)
e
200 nm
GLS2 + Pi
(30 seconds after adding substrate)
f
100 nm
GLS2 + Pi + 10 uM 968
(30 seconds after adding substrate)
g
200 nm
GLS2 N308A + Pi
(30 seconds after adding substrate)

769

770

771 **Figure 5. The proposed mechanism of glutaminase filament formation and dissociation.**
772 **(a)** The proposed mechanism for glutaminase filament formation and dissociation. Left: When
773 substrate binds, the lid (yellow) forms a 'lid lock', and the helical interface is exposed (shown in
774 gray), allowing the adjacent tetramer to extend the filament. Right: When product is released, the
775 lid loop becomes flexible, displacing the adjacent tetramer, and blocking the helical interface. **(b)**
776 Negative stain EM of GAC (Y466W) (1 μM) with inorganic phosphate (Pi, 200 mM) and DMSO
777 30 seconds after adding glutamine (substrate, 20 mM). **(c)** Negative stain EM of GAC (Y466W)
778 (1 μM) with Pi (200 mM) and DMSO 30 minutes after adding substrate (20 mM). **(d)** Negative-
779 stain EM of GAC (Y466W) (1 μM) with Pi (200 mM) and UPGL0004 (1 μM) 30 seconds after
780 adding substrate (20 mM). **(e)** Negative stain EM of GLS2 (1 μM) with Pi (50 mM) 30 seconds
781 after adding substrate (20 mM). **(f)** Negative stain EM of GLS2 (1 μM) with Pi (50 mM) and
782 compound 968 (10 μM) 30 seconds after adding substrate (20 mM). **(g)** Negative stain EM of
783 GLS2 (N308A) (1 μM) with Pi (50 mM) 30 seconds after adding substrate (20 mM).

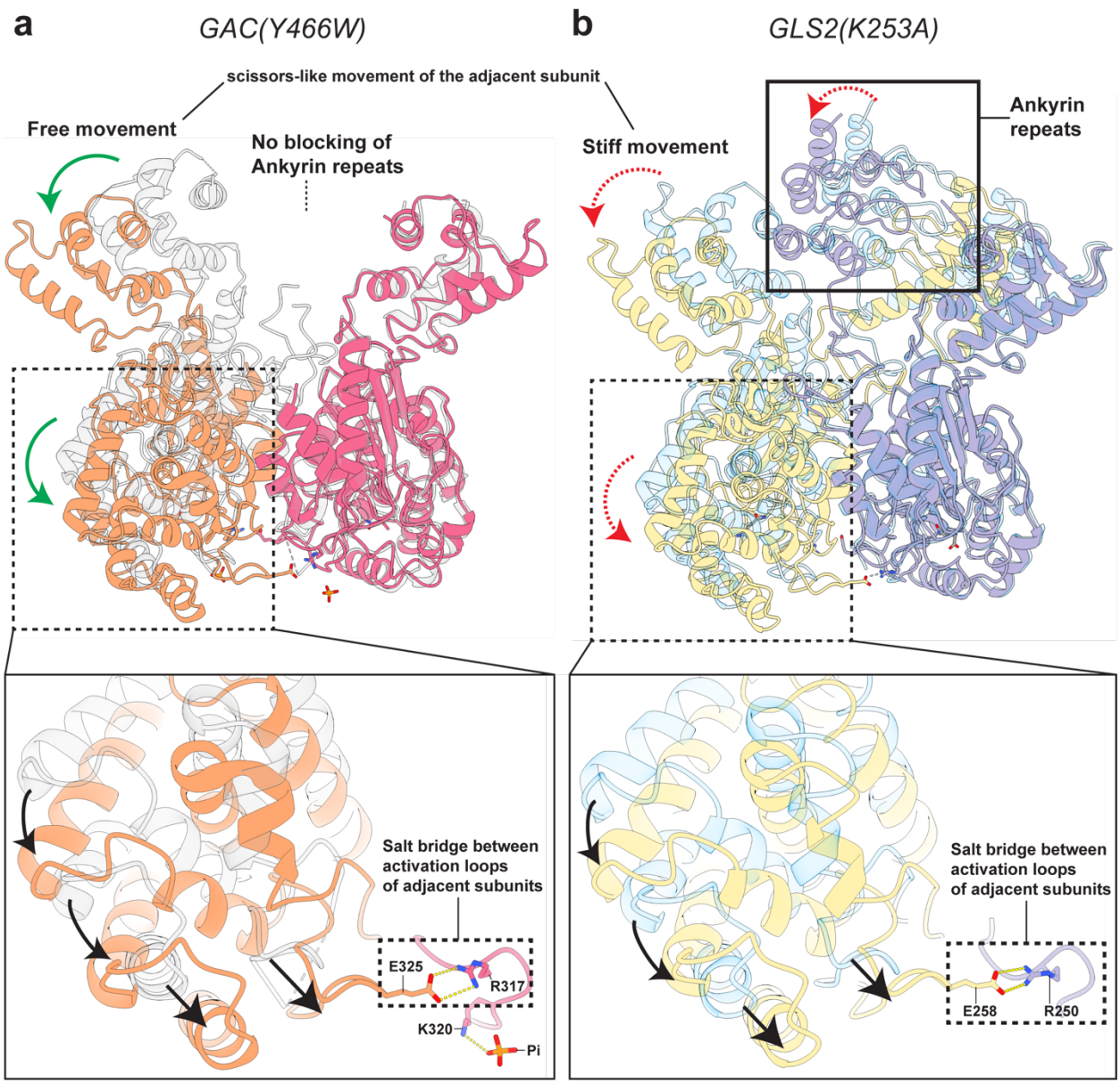
a
GAC(Y466W)
b
GLS2(K253A)
scissors-like movement of the adjacent subunit
Free movement
No blocking of
Ankyrin repeats
Stiff movement
Ankyrin
repeats
Salt bridge between
activation loops
of adjacent subunits
E325
R317
K320
Pi
Salt bridge between
activation loops
of adjacent subunits
E258
R250

784

785

786 **Figure 6. The proposed mechanism for regulation of GLS2 catalytic activity by the C-**
787 **terminal ankyrin repeats**.
788 **(a)** The unrestricted scissor-like movement of the N-terminal domain between monomers within a
789 dimer of the GAC filament (orange and magenta) and apo-GAC (light gray) after filament
790 formation. The arrows indicate the direction of conformational changes. Inset on the bottom: the
791 scissor-like movement brings Glu325 and Arg 317 from adjacent GAC monomers within a dimer
792 into close proximity and helps them form a salt bridge to stabilize the activation loops. **(b)** The
793 scissor-like movement of the N-terminal domain between monomers within a dimer of the GLS2
794 filament (purple and yellow) and apo-GLS2 (light blue) is restricted by the ankyrin repeats (solid
795 box). The arrows indicate the direction of conformational changes. The formation of the salt bridge
796 between Glu258 and Arg250 from adjacent GLS2 monomers within a dimer is burdened by the
797 blocking of ankyrin repeats, which prevents the activation loops contact at close proximity. Also,
798 see Extended Data Supplementary movie 1.

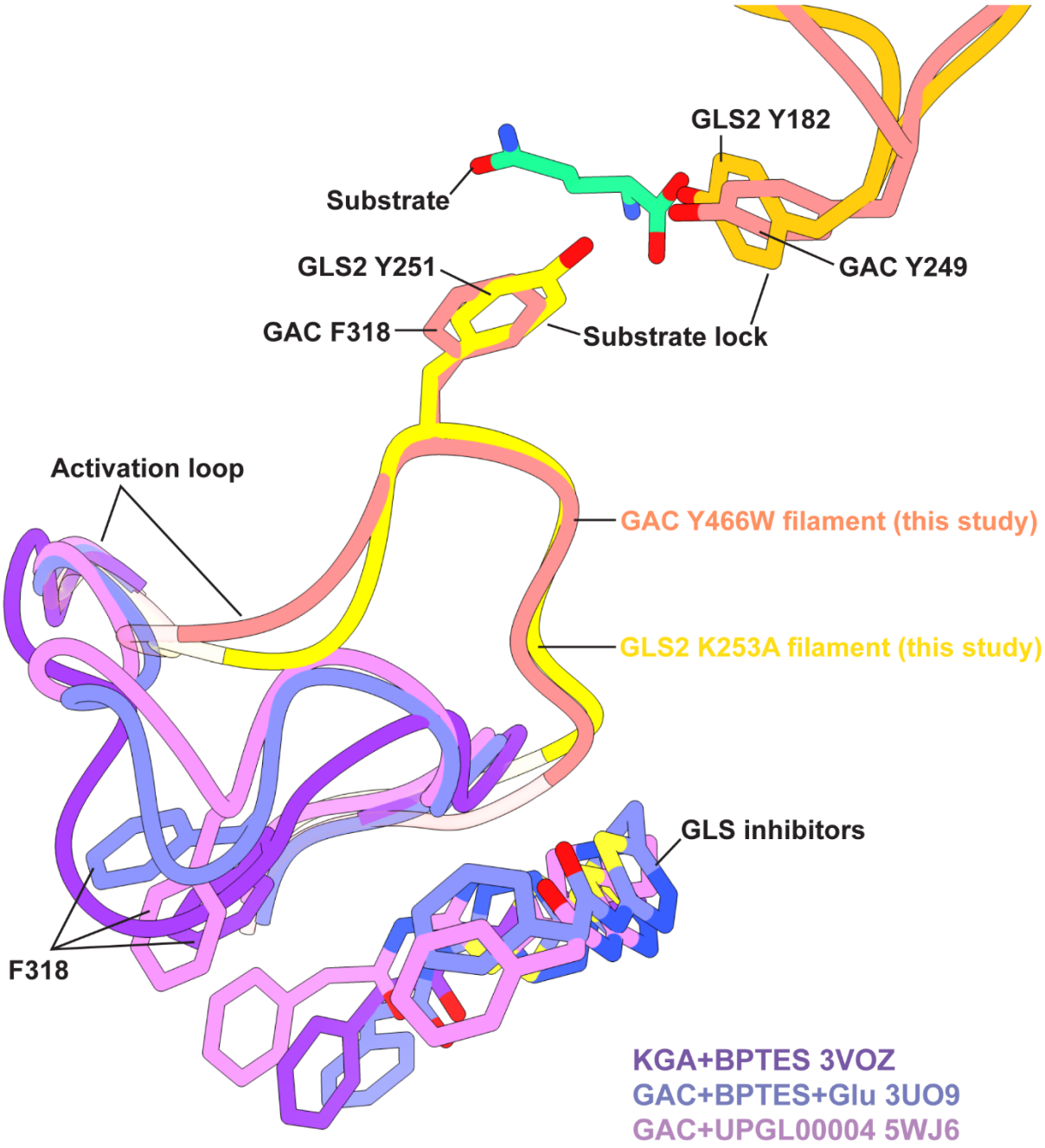
GLS2 Y182
Substrate
GLS2 Y251
GAC Y249
GAC F318
Substrate lock
Activation loop
GAC Y466W filament (this study)
GLS2 K253A filament (this study)
GLS inhibitors
F318
KGA+BPTES 3VOZ
GAC+BPTES+Glu 3UO9
GAC+UPGL00004 5WJ6

799

800

801 **Extended Data Figure 1.** The activation loops of the GAC (Y466W) filament (salmon), GLS2
802 (K253A) filament (yellow) and GAC bound to the allosteric inhibitors BPTES, alone or together
803 with glutamate, and UPGL0004 (purple, lavender and pink, respectively).

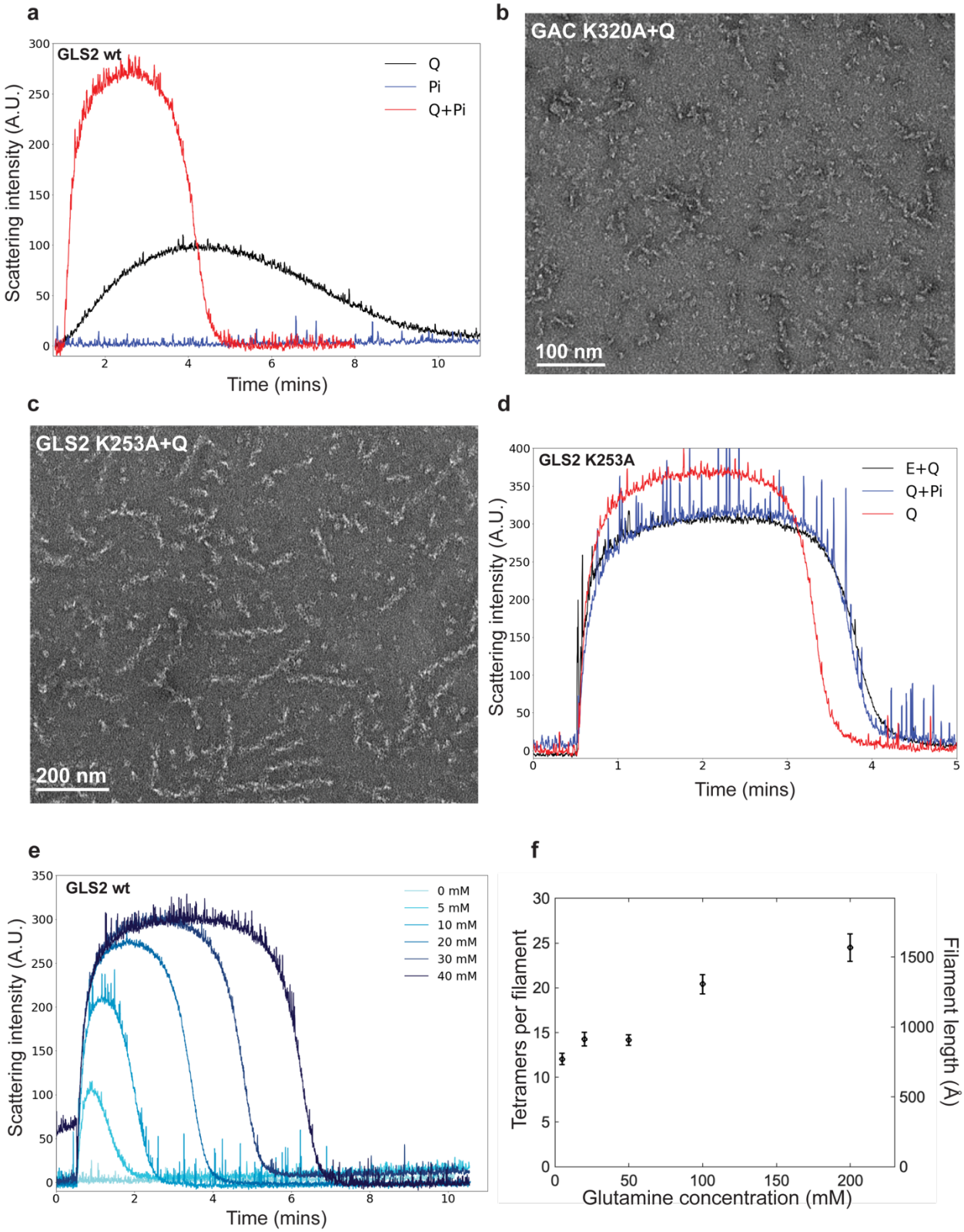
a
GLS2 wt
Q
Pi
Q+Pi
Scattering intensity (A.U.)
Time (mins)
b
GAC K320A+Q
100 nm
c
GLS2 K253A+Q
200 nm
d
GLS2 K253A
E+Q
Q+Pi
Q
Scattering intensity (A.U.)
Time (mins)
e
GLS2 wt
0 mM
5 mM
10 mM
20 mM
30 mM
40 mM
Scattering intensity (A.U.)
Time (mins)
f
Tetramers per filament
Filament length (Å)
Glutamine concentration (mM)

804

805 **Extended Data Figure 2. (a)** Right-angle light scattering (RALS) of GLS2 (2 μM) after the
806 addition of glutamine (Q, 20 mM), inorganic phosphate Pi (100 mM), or Q (20 mM) and Pi (100
807 mM). **(b)** Negative stain EM of GAC (K320A) (1 μM) after adding Q (20 mM). **(c)** Negative stain
808 EM of GLS2 (K253A) (1 μM) after adding Q (20 mM). **(d)** RALS of GLS2 (K253A) (2 μM) after
809 the addition of glutamate (E, 20 mM) and Q (20 mM) (black), Q (20 mM) (red), or Q (20 mM)
810 and Pi (100 mM) (blue). **(e)** RALS of GLS2 (2 μM) with Pi (100 mM) after the addition of
811 increasing concentrations of glutamine. **(f)** The average number of tetramers per filament plotted
812 against substrate (glutamine) concentration. The filament length was determined through an
813 analysis of negative stain electron microscopy images (n=3) with ImageJ. The width of each GLS2
814 tetramer is 64 Å, as measured from the high resolution cryo-EM structure of the GLS2 filament.
815 X-axis: the concentration of substrate (glutamine) in mM; left Y-axis: the number of tetramers per
816 filament; right Y-axis: the average length of filaments in Å. Circles indicate the mean value, and
817 error bars are shown for the standard error.
818

819

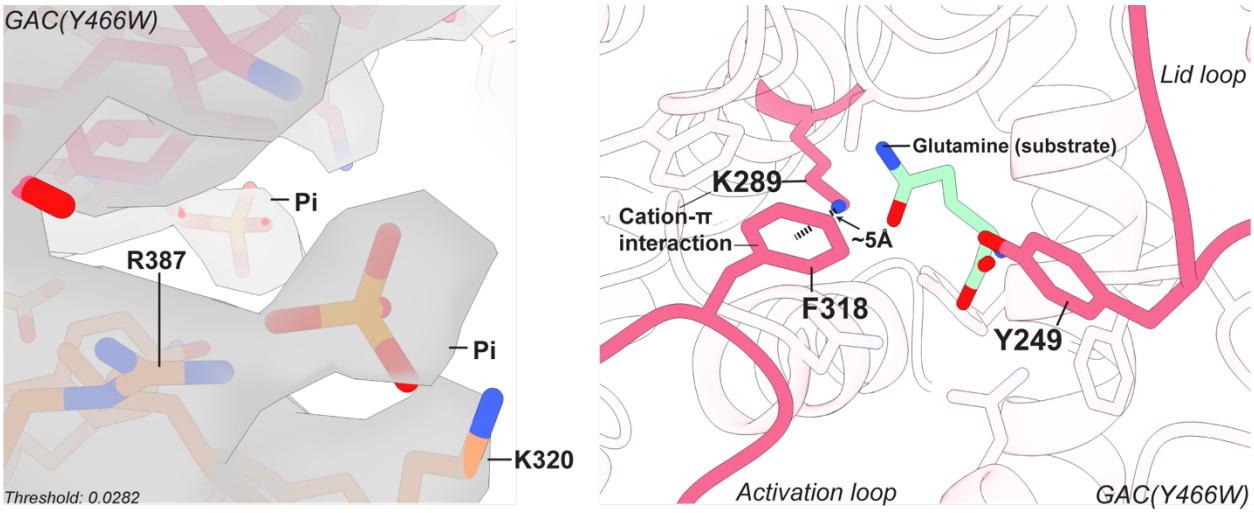
GAC(Y466W)
Pi
R387
Pi
K320
Threshold: 0.0282
Lid loop
Glutamine (substrate)
K289
Cation-π
interaction
~5Å
F318
Y249
Activation loop
GAC(Y466W)

820

821 **Extended Data Figure 3.** Left panel: the electron density of inorganic phosphate (Pi) bound near
822 the activation loop in the GAC (Y466W) filament. Right panel: the phenylalanine-tyrosine lock
823 in GAC consisting of Phe318 from the activation loop (magenta) and Tyr249 from the lid loop
824 (magenta). The substrate, glutamine, is shown in green. Lys289 interacts with Phe318 from the
825 activation loop through a cation-π interaction.

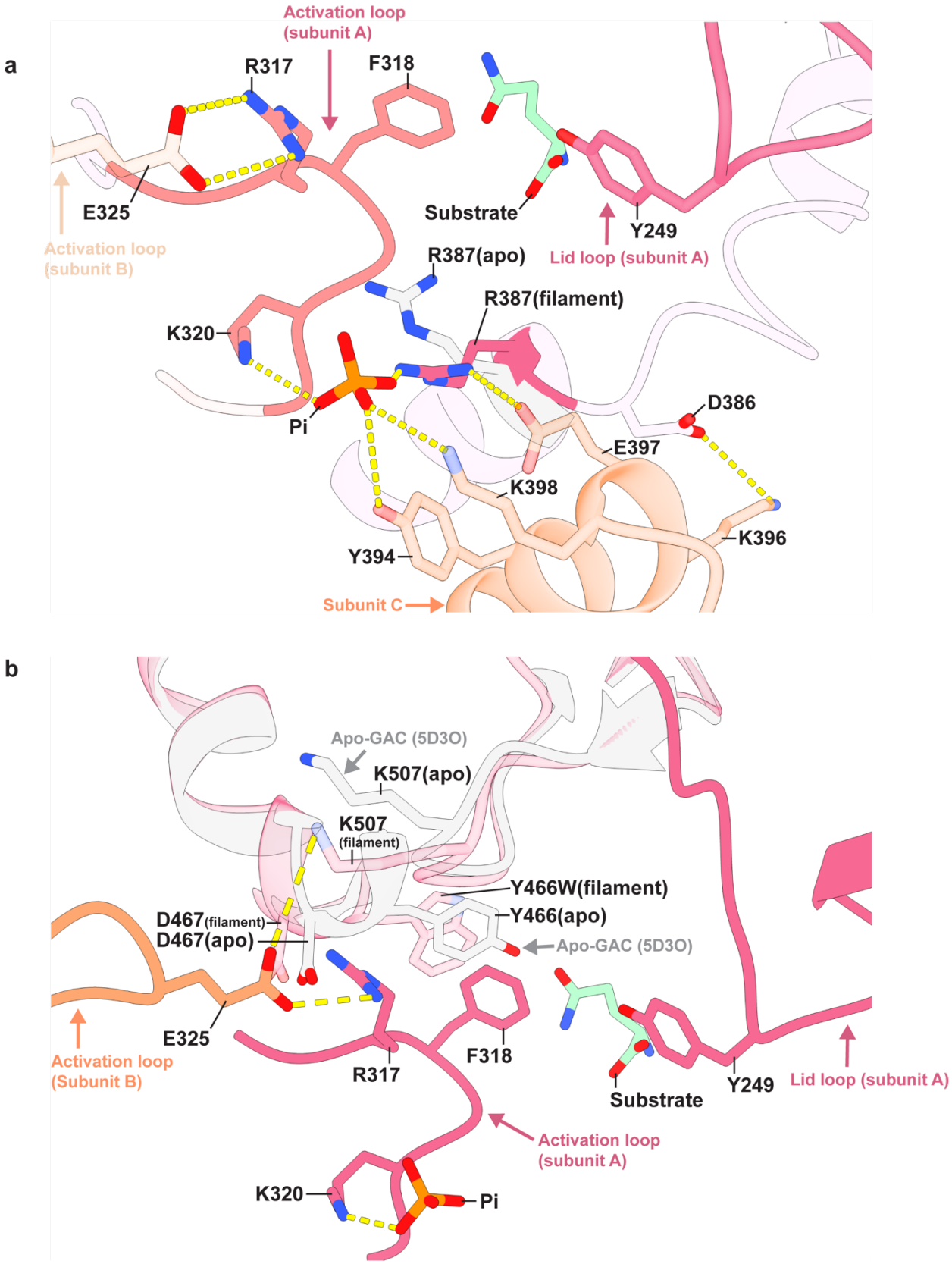
a
Activation loop
(subunit A)
R317
F318
E325
Activation loop
(subunit B)
Substrate
Y249
Lid loop (subunit A)
R387(apo)
R387(filament)
K320
Pi
D386
E397
K398
K396
Y394
Subunit C
b
Apo-GAC (5D3O)
K507(apo)
K507
(filament)
Y466W(filament)
Y466(apo)
D467(filament)
D467(apo)
Apo-GAC (5D3O)
E325
Activation loop
(Subunit B)
R317
F318
Substrate
Y249
Lid loop (subunit A)
Activation loop
(subunit A)
K320
Pi

826

827 **Extended Figure 4. (a)** The anionic activator, inorganic phosphate (Pi), interacts with Lys320 of
828 the activation loop, and Arg387, Tyr394, and Lys398 from the dimer-dimer interface of GAC
829 (Y466W), shown as yellow dashed lines. **(b)** The conserved residue in the active site, Tyr466, is
830 already inserted into the active site even without the new interaction between the Glu325 with
831 Asp467 and Arg317 that occurs within the filament structure.
832

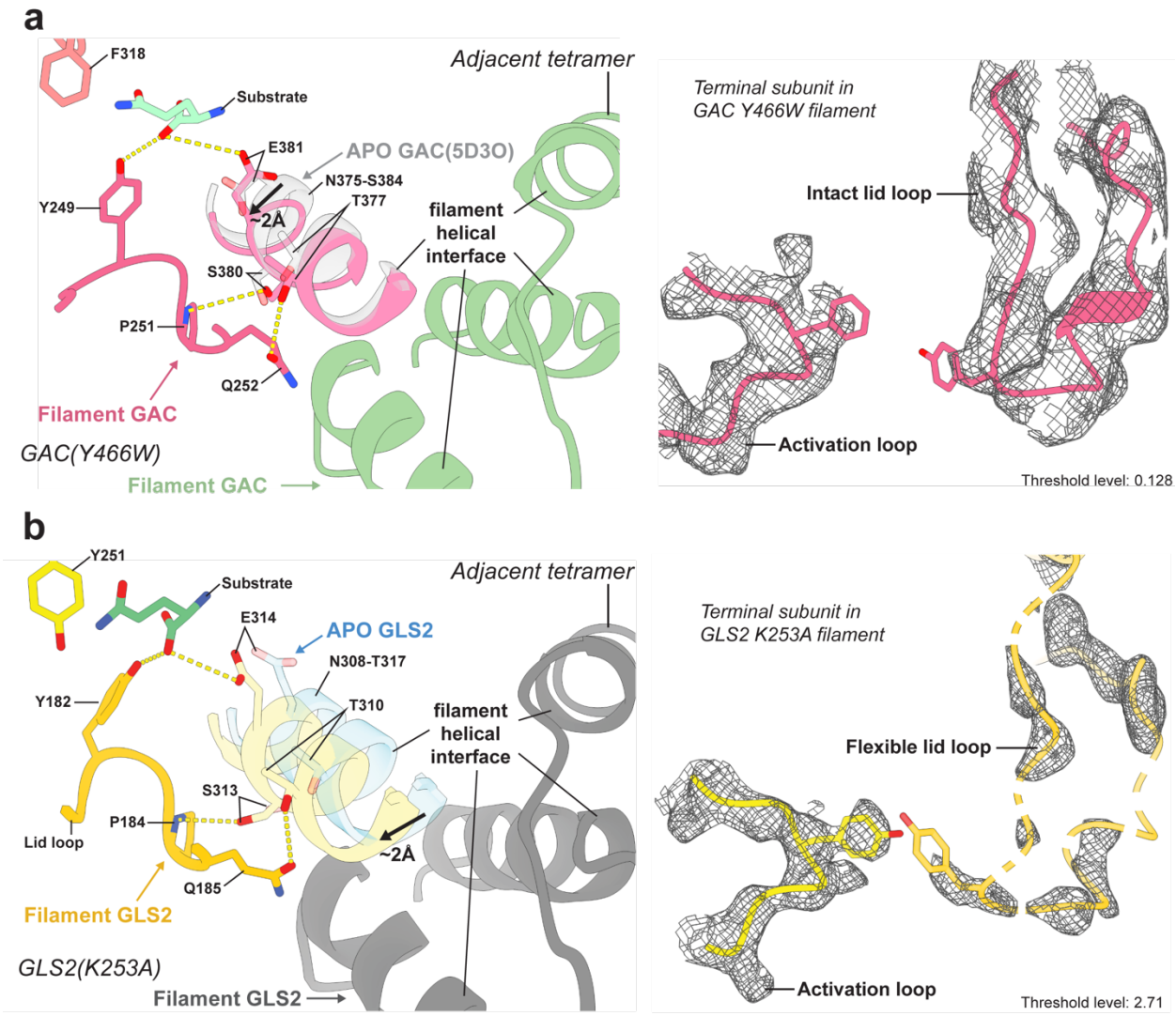
a
F318
Substrate
Adjacent tetramer
E381
APO GAC(5D3O)
N375-S384
T377
Y249
~2Å
filament
helical
interface
S380
P251
Q252
Filament GAC
GAC(Y466W)
Filament GAC
Terminal subunit in
GAC Y466W filament
Intact lid loop
Activation loop
Threshold level: 0.128
b
Y251
Substrate
Adjacent tetramer
E314
APO GLS2
N308-T317
Y182
T310
filament
helical
interface
S313
P184
Lid loop
~2Å
Q185
Filament GLS2
GLS2(K253A)
Filament GLS2
Terminal subunit in
GLS2 K253A filament
Flexible lid loop
Activation loop
Threshold level: 2.71

833

834

835 **Extended Data Figure 5. (a)** Left panel: the lid loop of GAC is stabilized in the active
836 conformation by a lid lock involving the lid loop and residues adjacent to the filament helical
837 interface between tetramers within the filament. Hydrogen bonds are indicated by yellow dashed
838 lines. Apo-GAC is light gray, and the GAC filament is shown in magenta. The adjacent tetramer
839 in the filament is shown in green. The arrow indicates the direction of the conformational change.
840 Right panel: the cryo-EM density map of the lid loop of the terminal subunit in the GAC filament.
841 The lid loop in the catalytic-deficient GAC (Y466W) filament has strong density in its terminal
842 subunit. **(b)** Left panel: the lid loop of GLS2 is stabilized in the active conformation through a lid
843 lock. Hydrogen bonds are indicated by yellow dashed lines. Apo-GLS2 is light blue and the GLS2
844 filament is shown in yellow and orange. The adjacent tetramer that is forming the helical interface
845 is shown in dark gray. The arrow indicates the direction of the conformational change. Right panel:
846 the cryo-EM density map of the lid loop of the terminal subunit in the GLS2 filament. The weak
847 density of the lid loop in the terminal tetramer of GLS2 suggests increased flexibility compared to
848 the lid loops in the other tetramers that make up the filament.

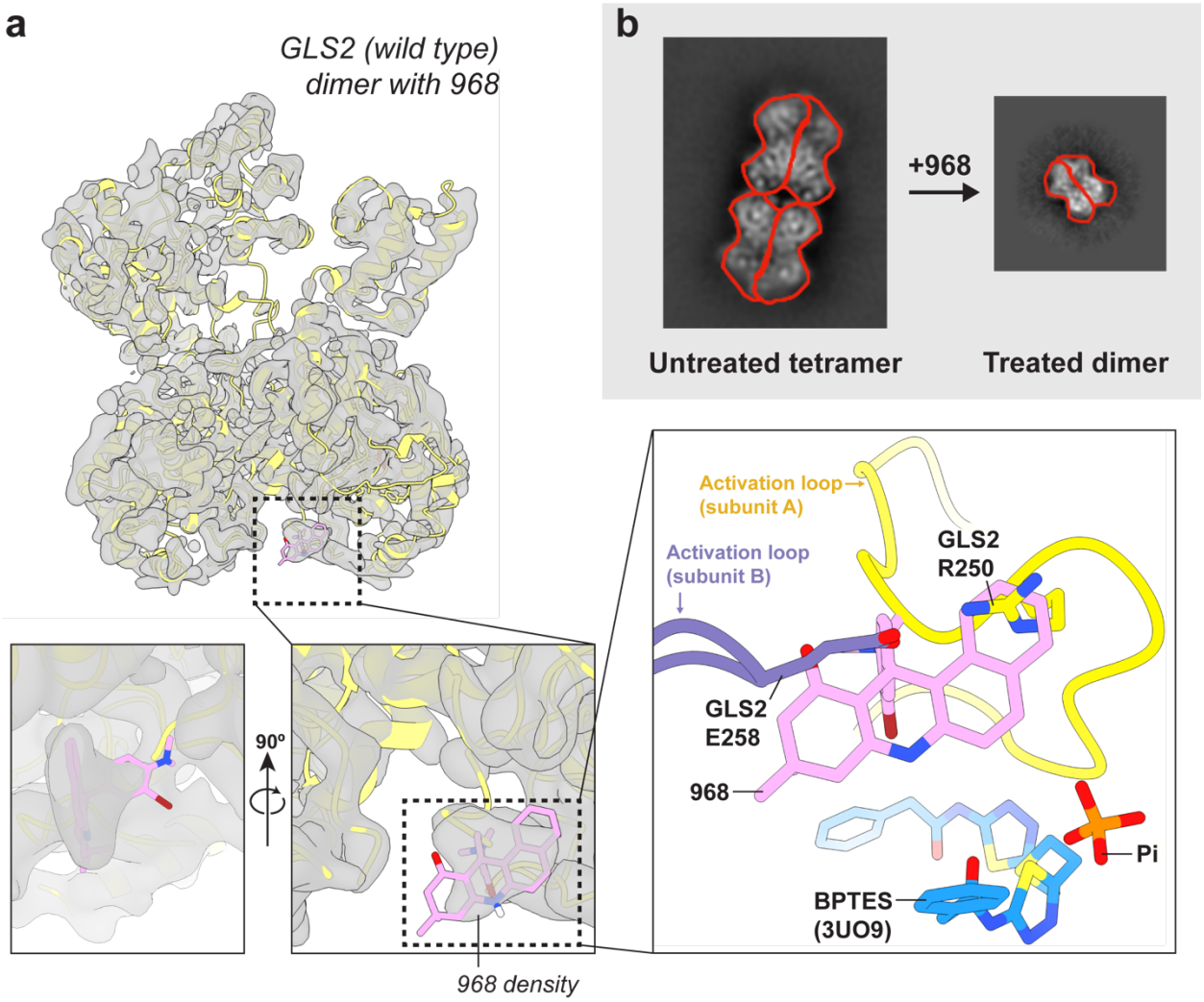
a
GLS2 (wild type)
dimer with 968
90°
968 density
b
+968
Untreated tetramer
Treated dimer
Activation loop
(subunit A)
Activation loop
(subunit B)
GLS2
R250
GLS2
E258
968
Pi
BPTES
(3UO9)

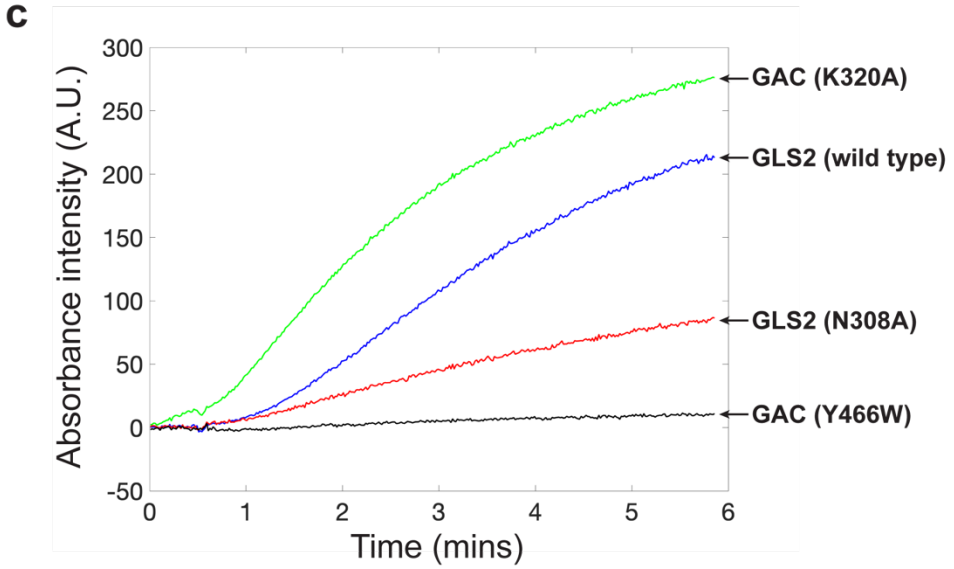
c
Absorbance intensity (A.U.)
300
250
200
150
100
50
0
-50
0
1
2
3
4
5
6
Time (mins)
GAC (K320A)
GLS2 (wild type)
GLS2 (N308A)
GAC (Y466W)

849

850 **Extended Data Figure 6. (a)** Upper left: the 3D reconstruction of wild type GLS2 bound to 968.
851 Bottom left inset: The electron density for 968 suggests that it interacts with the activation loops.
852 Bottom right inset: The relative positions of 968, BPTES, and inorganic phosphate (Pi) are shown.
853 Notably, 968 interferes with the interaction between Arg250 on one activation loop and Glu258
854 on an adjoining activation loop. **(b)** cryo-EM 2D classification of GLS2 treated with 968 shows
855 that approximately 10% of the particles can be found as dimers in the presence of 968, whereas no
856 dimers are detected in the absence of 968. Each monomer depicting the GLS2 tetramer and dimer
857 is outlined in red. **(c)** The fluorescence trace of the activity assay of GLS2 (N308A) compared with
858 wild type GLS2, GAC (Y466W), and GAC (K320A). Assays of glutaminase activity were
859 performed as previously described[25]. X-axis: time in minutes; Y-axis: the intensity of the
860 absorbance at 340 nm, which is proportional to the yield of catalytic product. The concentrations
861 of GLS2 (N308A), wild type GLS2 and GAC (Y466W) used in these experiments were 0.6 μM,
862 and the concentration of GAC (K320A) was 0.12 μM. The concentration of glutamine in these
863 assays was 20 mM. The concentration of inorganic phosphate was 50 mM when assaying the
864 catalytic activity of GLS2 and GLS2 (N308A), and 200 mM when assaying GAC (Y466W) and
865 GAC (K320A).

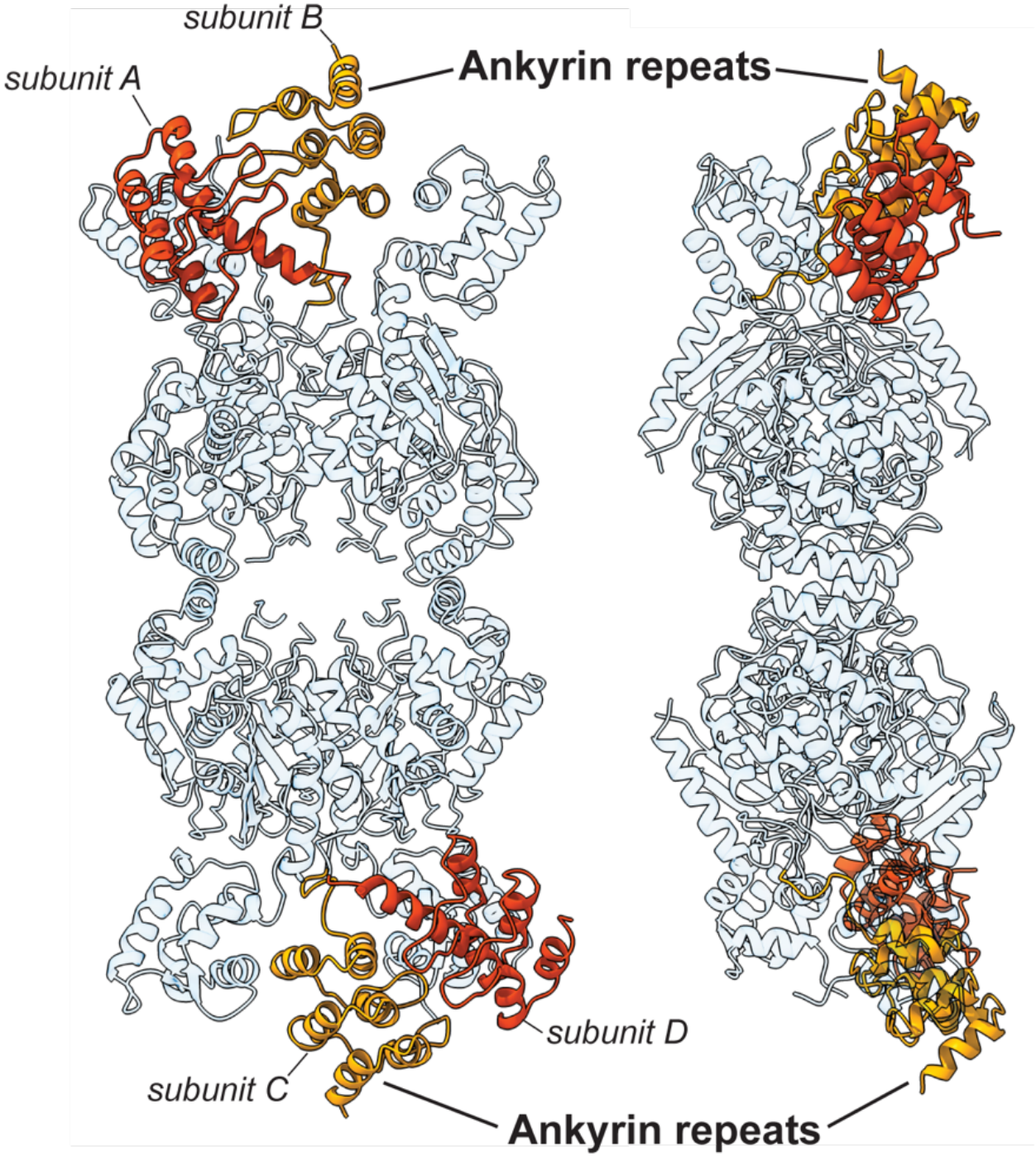
subunit B
subunit A
Ankyrin repeats
subunit D
subunit C
Ankyrin repeats

868 **Extended Data Figure 7.** The asymmetric positioning of the ankyrin repeats in apo-GLS2 from

869 different subunits shown in orange and yellow.

870

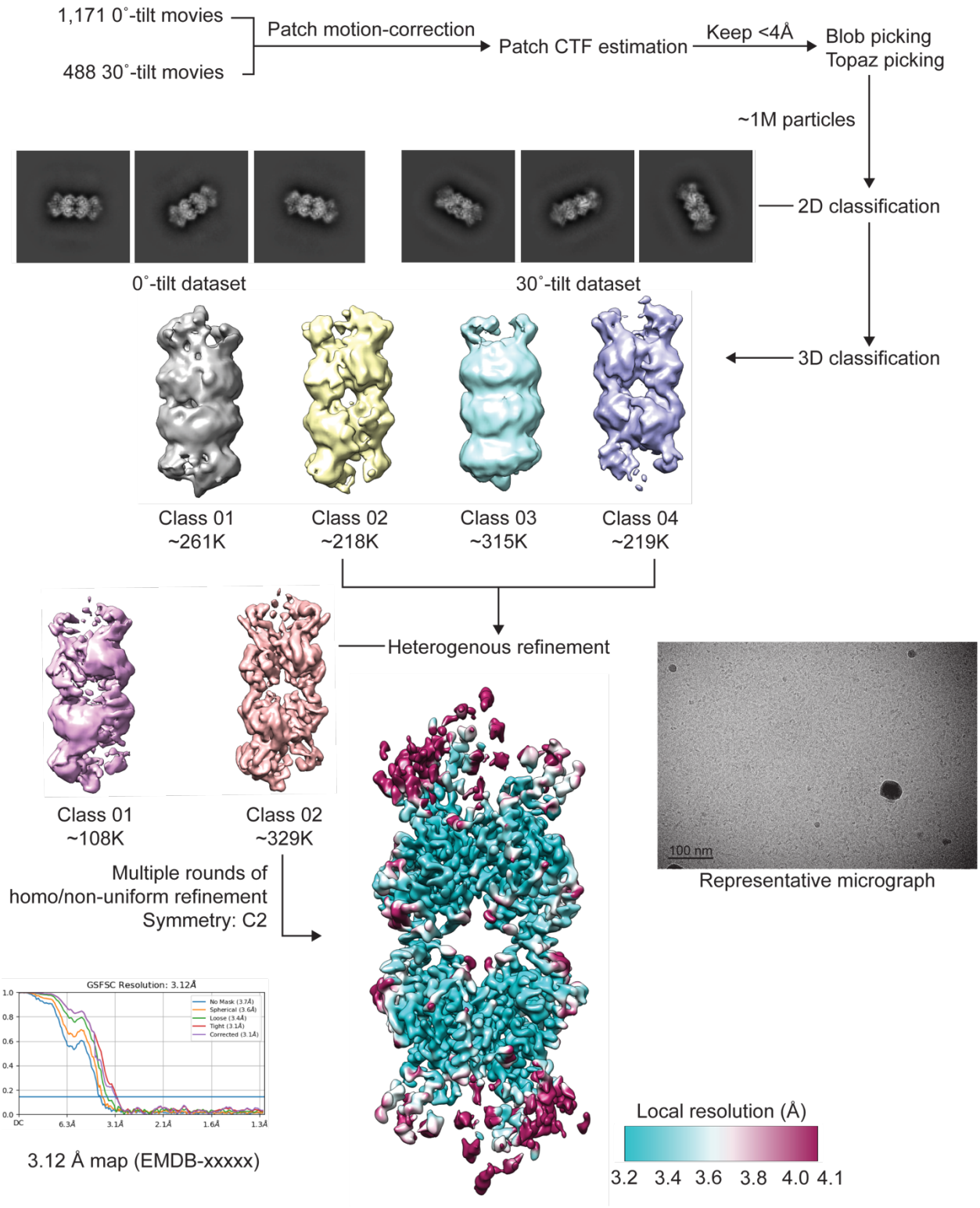
1,171 0˚-tilt movies
488 30˚-tilt movies
Patch motion-correction
Patch CTF estimation
Keep <4Å
Blob picking
Topaz picking
~1M particles
2D classification
0˚-tilt dataset
30˚-tilt dataset
3D classification
Class 01
~261K
Class 02
~218K
Class 03
~315K
Class 04
~219K
Heterogenous refinement
Class 01
~108K
Class 02
~329K
Multiple rounds of
homo/non-uniform refinement
Symmetry: C2
100 nm
Representative micrograph
GSFSC Resolution: 3.12Å
No Mask (3.7Å)
Spherical (3.6Å)
Loose (3.4Å)
Tight (3.1Å)
Corrected (3.1Å)
DC
6.3Å
3.1Å
2.1Å
1.6Å
1.3Å
3.12 Å map (EMDB-xxxxx)
Local resolution (Å)
3.2 3.4 3.6 3.8 4.0 4.1

873 **Extended Data Figure 8.** The cryo-EM data processing workflow of apo-GLS2.

874

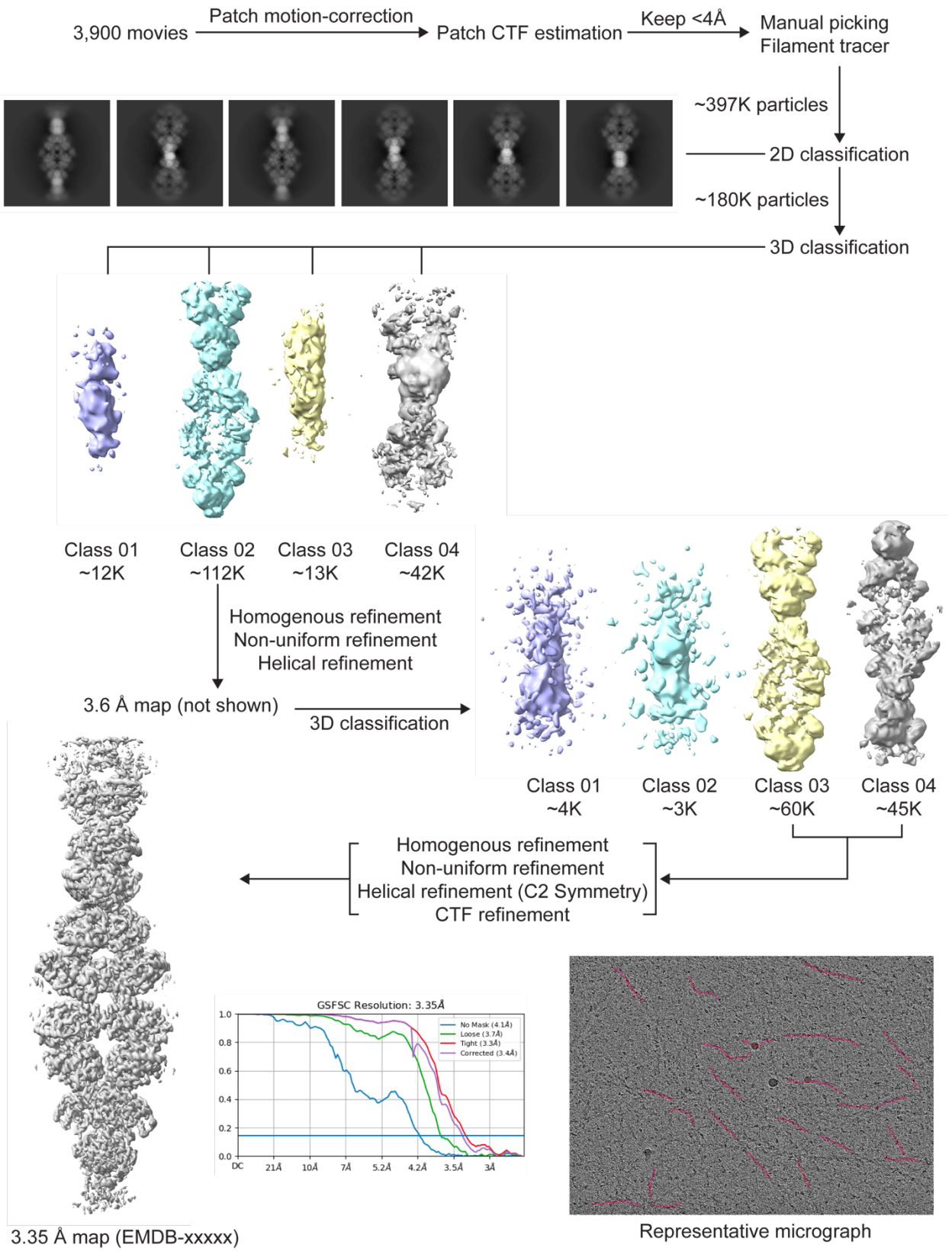
3,900 movies
Patch motion-correction
Patch CTF estimation
Keep <4Å
Manual picking
Filament tracer
~397K particles
2D classification
~180K particles
3D classification
Class 01
~12K
Class 02
~112K
Class 03
~13K
Class 04
~42K
Homogenous refinement
Non-uniform refinement
Helical refinement
3.6 Å map (not shown)
3D classification
Class 01
~4K
Class 02
~3K
Class 03
~60K
Class 04
~45K
Homogenous refinement
Non-uniform refinement
Helical refinement (C2 Symmetry)
CTF refinement
GSFSC Resolution: 3.35Å
No Mask (4.1Å)
Loose (3.7Å)
Tight (3.3Å)
Corrected (3.4Å)
1.0
0.8
0.6
0.4
0.2
0.0
DC
21Å
10Å
7Å
5.2Å
4.2Å
3.5Å
3Å
3.35 Å map (EMDB-xxxxx)
Representative micrograph

877 **Extended Data Figure 9.** The cryo-EM data processing workflow of GAC Y466W filament.

878

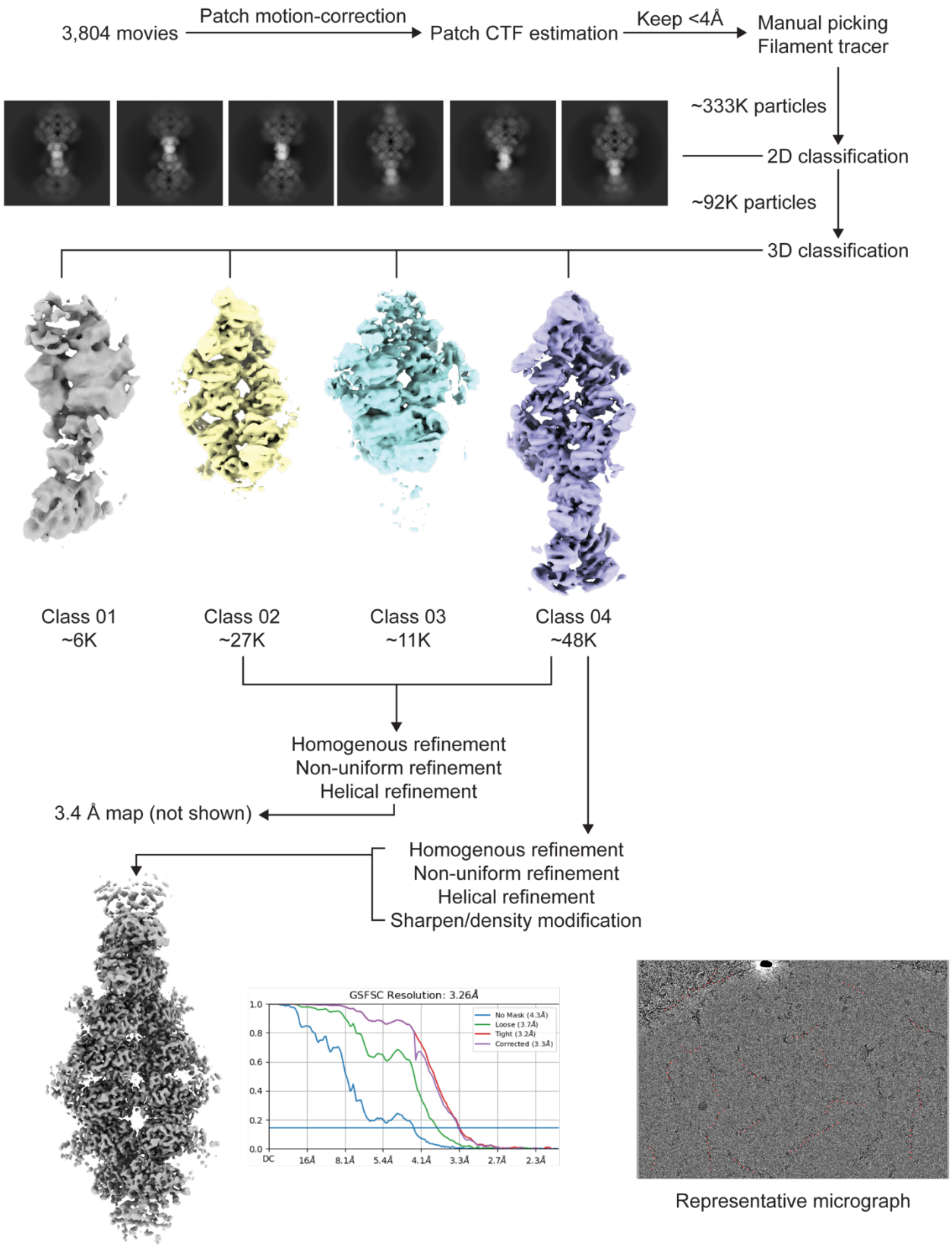
3,804 movies
Patch motion-correction
Patch CTF estimation
Keep <4Å
Manual picking
Filament tracer
~333K particles
2D classification
~92K particles
3D classification
Class 01
~6K
Class 02
~27K
Class 03
~11K
Class 04
~48K
Homogenous refinement
Non-uniform refinement
Helical refinement
3.4 Å map (not shown)
Homogenous refinement
Non-uniform refinement
Helical refinement
Sharpen/density modification
GSFSC Resolution: 3.26Å
No Mask (4.3Å)
Loose (3.7Å)
Tight (3.2Å)
Corrected (3.3Å)
1.0
0.8
0.6
0.4
0.2
0.0
DC
16Å
8.1Å
5.4Å
4.1Å
3.3Å
2.7Å
2.3Å
Representative micrograph
3.26 Å map (EMDB-xxxxx)

879

880 **Extended Data Figure 10.** The cryo-EM data processing workflow of GLS2 K253A filament.

881 **Extended Data Table 1. Cryo-EM data collection, refinement and validation statistics.**
882

	Apo GLS2 (EMD-40920) (PDB 8SZL)	GAC(Y466W) filament (EMD-40918) (PDB 8SZJ)	GLS2(K253A) filament (EMD-40950) (PDB 8T0Z)
Data collection and processing			
Magnification	63kx	63kx	81kx
Voltage (kV)	200	200	300
Electron exposure (e–/Å^2)	50	50	50
Defocus range (μm)	-0.8~-2.0	-0.8~-2.0	-0.8~-2.0
Physical pixel size (Å)	1.23	1.31	1.058
Symmetry imposed	C2	C2	C1
Initial particle images (no.)	~1M	~397K	~333K
Final particle images (no.)	~329K	~45K	~49K
Map resolution (Å)	3.12	3.35	3.26
FSC threshold	0.143	0.143	0.143
Map resolution range (Å)	3.0-5.0	3.1-5.0	3.0-5.0
Refinement			
Initial model used (PDB code)	4BQM	4BQM	4BQM
Model resolution (Å)	3.12	3.35	3.26
FSC threshold	0.143	0.143	0.143
Model resolution range (Å)	3.0-5.0	3.0-5.0	3.0-5.0
Map sharpening *B* factor (Å^2)	164.90	112.1	211.56
Model composition			
Non-hydrogen atoms	15,095	36,204	47,436
Protein residues	1,961	4,656	6,108
Ligands	0	24	12
B factors (Å^2)			
Protein	164.90	189.44	211.56
Ligand	N/A	173.39	N/A
R.m.s. deviations			
Bond lengths (Å)	0.003	0.002	0.005
Bond angles (°)	0.553	0.647	0.671
Validation			
MolProbity score	2.01	1.89	2.02
Clashscore	11.86	10.20	11.00
Poor rotamers (%)	0.06	0.67	0.69
Ramachandran plot			
Favored (%)	93.70	94.74	92.59
Allowed (%)	6.30	5.13	7.31
Disallowed (%)	0.00	0.13	0.10

883